Mon. Not. R. astr. Soc. (1992) **257**, 545–571

Spectral ageing in a sample of 14 high-luminosity double radio sources

Ronghui Liu,* Guy Pooley and Julia M. Riley
Mullard Radio Astronomy Observatory, Cavendish Laboratory, Madingley Road, Cambridge CB3 0HE

Accepted 1992 February 12. Received 1992 February 11; in original form 1991 December 20

SUMMARY

We use multifrequency observations of a sample of 14 high-luminosity 3C double radio sources in a discussion of their structures and spectral properties. The observations were made with the VLA at 1.4, 5 and 15 GHz and have resolutions of 0.4 or 1.2 arcsec. We interpret the spectra in terms of the ageing of the electron population, as in the related study by Alexander & Leahy. The hotspots always have the youngest population of electrons, and the apparent ages increase away from the hotspot, even in those cases where the diffuse emission extends perpendicular to the source axis or directly away from the nucleus.

Key words: galaxies: active – radio continuum: galaxies.

1 INTRODUCTION

According to the standard beam model for FRII (Fanaroff & Riley 1974) sources, electrons in the hotspot region have been more recently accelerated, or are younger in terms of their synchrotron lifetime, than those in the radio lobe (Blandford & Rees 1974). Provided that there is no significant reacceleration within the lobes and no significant mixing of particles, there should be a spectral gradient across the radio source with the spectrum of the radiation from the lobe being steeper than that at the hotspot. This picture has been confirmed by many observations – the hotspots always have flatter spectra than the lobes and the spectra steepen continuously away from the hotspots along the lobes (Burch 1977, 1979; Mayer 1979; Winter *et al.* 1980; Alexander, Brown & Scott 1984; Myers & Spangler 1985; Alexander 1987; Alexander & Leahy 1987; Leahy, Muxlow & Stephens 1989). Synchrotron-loss models are fitted well by multifrequency observations, giving information about the synchrotron lifetime of the electrons and providing a characteristic speed which represents the rate of separation of the hotspot and the lobe material. Recent results showing systematic asymmetries in the spectral-index distributions (Liu & Pooley 1991a, b) have not changed the basic model.

Alexander & Leahy (1987, hereafter AL) studied a sample of 3C double radio galaxies. They found that the apparent separation speeds ranged up to $0.2c$, and that the speeds increase with luminosity. AL's sample was limited to FRII sources with angular size $\theta \geq 45$ arcsec, and consequently most of their sources have $P_{178} \leq 10^{28}$ W Hz^{-1} sr^{-1}. We extend the work of AL to a complete sample of 14 high-luminosity double sources. In Sections 2 and 3 we describe the sample selection, the observations and the data reduction. In Section 4 we outline the spectral index and spectral ageing analysis. The results are presented in Section 5. Discussion of the results is given in Section 6 and the conclusions are summarized in Section 7. We adopt a Friedmann cosmology with $H_0 = 50$ km s^{-1} Mpc^{-1} and $q_0 = 0$, and the convention $S_\nu \propto \nu^{-\alpha}$.

2 THE SAMPLE

The sources analysed by AL and those discussed in this paper form a subset of the well-defined sample of bright sources selected by Laing, Riley & Longair (1983). They have $\delta > 10°$, $|b| > 50°$ and angular size $\theta > 4$ arcsec and are all unambiguous FRII sources having $P_{178} \geq 10^{25}$ W Hz^{-1} sr^{-1}.

There are 34 sources in all. 15 of these have $\theta \geq 45$ arcsec and the spectral ageing has been studied by AL. 3C236 has $\theta \geq 2440$ arcsec which is too large to be mapped with the aperture coverage available. 3C263, 267, 295 and 303 are excluded due to scheduling errors and technical problems during the observations. These omissions are unlikely to affect the conclusions. The remaining 14 sources form the current high-luminosity sample. They are listed in Table 1.

The selection criteria impose some correlations on the data. First, the redshift and luminosity are correlated because this is a flux-limited sample. Secondly the largest angular size and luminosity are anticorrelated (Fig. 1a), the smaller sources tending to be more luminous. Fig. 1(b) shows the distribution of the sources in the power–linear size ($P-D$) plane.

3 OBSERVATIONS AND DATA REDUCTION

All the observations of the current sample were made with the Very Large Array (VLA) between 1988 May and 1989 March. In order to carry out a systematic multifrequency

* Present address: Mullard Space Science Laboratory, Holmbury St Mary, Dorking, Surrey RH5 6NT.

study of these double sources with a minimum of 10 beamwidths along the source, we made scaled-array observations at three frequencies where possible (1.4, 5 and 15 GHz), requiring three array configurations (A, B and C). The details are presented in Table 2.

As it is important to have adequate aperture coverage to obtain a suitable dynamic range for the mapping of relatively faint lobe structure, we made two 10-min snapshot observations of each source at well separated hour angles in each configuration and at each frequency. Calibration followed normal VLA practice, with calibration sources observed approximately every half-hour. Further observational details on individual sources are given in Table 3.

The data were edited and calibrated using the standard DEC10 programs then available at the VLA. Subsequent reduction was performed with the AIPS package (Fomalont & Bridle 1983). All the maps have been cleaned and self-calibrated. For later multifrequency comparison, the higher frequency data were normally self-calibrated on the first iteration using the set of clean components derived from the nearest lower frequency data of the same source at a comparable resolution. This process ensures that the maps at different frequencies are aligned to within a small fraction of a beamwidth. In those cases where this procedure was not followed, the high-frequency maps were shifted (in the worst case by 0.1 of a beamwidth) to align them with the lower frequency maps. For a few of the most extended sources, the longer baselines are undersampled, so a Gaussian weighting was applied to the aperture plane, reducing the resolution until the images were dominated by the densely sampled shorter baselines. The final clean maps were restored with circular Gaussian beams and the half-power beamwidths are listed in Table 3. The rms noise, σ, is typically 0.2, 0.12 and 0.35 mJy at 1.4, 5 and 15 GHz respectively.

Table 1. The sample.

Source	z	$\log(P_{178}/\mathrm{W\ Hz^{-1}\ sr^{-1}})$	θ (arcsec)	D (kpc)	ID
3C239	1.79	28.75	13.0	165	g
3C245	1.029	28.02	8.0	88	q
3C247	0.749	27.49	16.7	164	g
3C254	0.734	27.83	17.0	165	q
3C263.1	0.824	27.90	8.2	85	g
3C266	1.275	28.23	5.9	69	g
3C268.4	1.400	28.23	11.6	139	q
3C270.1	1.519	28.43	12.5	154	q
3C275.1	0.557	27.50	22.0	189	q
3C280	0.996	28.20	17.7	193	g
3C288	0.246	26.68	23.0	120	g
3C289	0.967	27.88	11.8	128	g
3C294	1.779	28.64	22.0	281	g
3C299	0.367	26.83	13.0	90	g

4 SPECTRAL ANALYSIS

4.1 Multifrequency comparison

For the purpose of comparing them, the maps at different frequencies are convolved to a common resolution, using a map-plane convolution. There are basically two sets of resolutions: resolution (1) is about 1.2 arcsec with 0.3-arcsec

Table 2. VLA observations.

Observing date	May 1988	Jan. 1989	March 1989
Configuration	C	A	B
Frequency(MHz)	14965	4885, 1465	14965, 4885
Bandwidth(MHz)		50	
Calibrators		3C286, 1144+402	
Flux scale		Baars et al. (1977)	

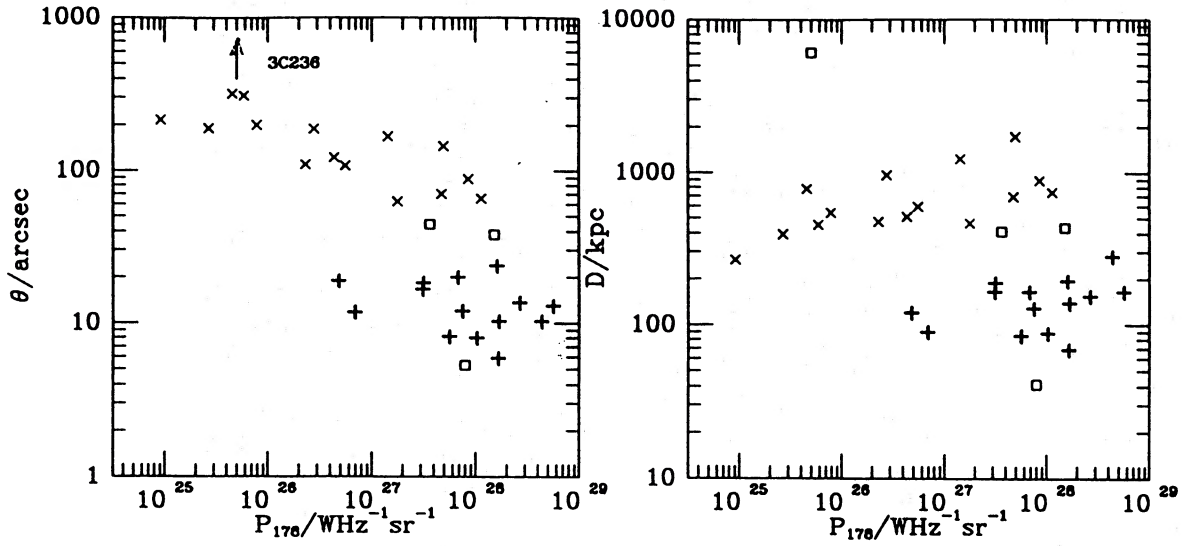

Figure 1. Distributions of the sample in (a) the $P-\theta$ and (b) the $P-D$ planes. The thin crosses (×) are sources in the sample of AL; bold crosses (+) are the current sample; open squares (□) are sources which have been excluded from the sample for reasons discussed in the text.

Table 3. Observational parameters and observed properties of individual sources.

Source	Map centre (B1950.00) RA	Dec	Freq. (GHz)	Array	HPBW(arcsec) (1)	(2)	Noise (mJy)	$S^{(a)}_{\text{total}}$ (Jy)	$S^{(b)}_{\text{LP}}$ (Jy)
3C239	$10^h08^m39.^s38$	$46^0 43' 11.''4$	1.4	A	1.15	-	0.2	1.52	1.461
			5	A, B	1.15	0.40	0.25	0.29	0.328
			15	B	1.15	0.45	0.07	0.042	0.080
3C245	10 40 06. 06	12 19 09. 4	5	A	-	0.37	0.35	1.71	1.380
			15	B	-	0.48	0.27	0.91	0.850
3C247	10 56 08. 09	43 17 27. 4	1.4	A	1.10	-	0.45	2.83	2.953
			5	B	1.25	-	0.17	0.87	0.943
3C254	11 11 53. 11	40 53 41. 7	1.4	A	1.25	-	0.33	2.96	3.252
			5	B	1.20	-	0.12	0.747	0.784
3C263.1	11 40 49. 39	22 23 35. 8	5	A	-	0.35	0.1	0.79	0.775
			15	B	-	0.45	0.3	0.216	-
3C266	11 43 04. 39	50 02 47. 2	5	A	-	0.31	0.07	0.31	0.318
			15	B	-	0.45	0.3	0.058	0.120
3C268.4	12 06 41. 99	43 56 01. 0	1.4	A	1.33	-	0.33	1.98	2.068
			5	A, B	1.33	0.43	0.16	0.60	0.596
			15	B, C	1.20	0.40	0.2	0.18	0.180
3C270.1	12 18 03. 88	33 59 48. 6	1.4	A	1.25	-	0.4	2.768	2.727
			5	A, B	1.25	0.40	0.3	0.80	0.864
			15	B, C	1.25	0.45	0.16	0.27	0.440
3C275.1	12 41 27. 86	16 39 13. 5	1.4	A	1.20	-	0.3	2.73	2.953
			5	B	1.54	-	0.12	1.01	0.904
3C280	12 54 41. 33	47 36 31. 6	1.4	A	1.08	-	0.5	5.10	5.124
			5	B	1.15	-	0.15	1.70	1.519
			15	C	1.18	-	1.0	0.57	0.520
3C288	13 36 38. 64	39 06 24. 4	1.4	A	1.28	-	0.25	2.67	3.406
			5	B	1.28	-	0.07	0.84	0.983
3C289	13 43 27. 72	50 01 31. 4	1.4	A	1.20	-	0.3	2.34	2.346
			5	A, B	1.20	0.40	0.07	0.633	0.596
			15	B, C	1.20	0.45	0.25	0.167	0.180
3C294	14 04 34. 12	34 25 39. 5	1.4	A	1.15	-	0.15	1.23	1.358
			5	B	1.15	-	0.06	0.26	0.278
			15	C	1.40	-	0.4	0.053	0.060
3C299	14 19 06. 38	41 58 30. 9	1.4	A	1.15	-	0.5	2.95	3.056
			5	A, B	1.15	0.40	0.1	0.925	0.894
			15	B, C	1.15	0.45	0.7	0.26	0.260

[a]and [b] are integrated flux densities from our measurements and those of Laing & Peacock (1980).

sampling, and resolution (2) 0.4 arcsec with 0.1 arcsec per grid point. Seven sources only have two-frequency maps at one of the resolutions. The other seven have low-resolution maps at all three frequencies, and most of them also have high-resolution maps at the two higher frequencies.

The central components have not been removed because of the lack of information on some of the cores. Thus, in some sources, the spectra near the radio core tend to become flatter due to the core emission.

4.2 Spectral index analysis

The mean spectral indices of the lobes were determined from integrals of total intensity along strips perpendicular to the lobe axes. The particular axes chosen in each case are shown as dashed lines on the first of each set of contour maps (Figs 4–17). The strips are one beamwidth across, and the integration stops when the intensity falls to 3σ (or, in the case of contorted sources like 3C247, at an arbitrary division between the parts of the lobe).

The uncertainties in the strip spectral indices determined in this way are estimated as follows.

(i) Random error. Random errors in the spectral-index calculations arise from the random noise. The effects are more important in the faint lobes than in the hotspot regions, but are never more than 15 per cent (giving rise to a maximum value of $\Delta\alpha/\alpha \sim 0.15$).

(ii) Systematic errors in the flux density scales at the three frequencies. By comparison of our integrated flux densities with those of Laing & Peacock (1980, LP), we find that our measurements are about 2.5 per cent less than those of LP at both 1.4 and 5 GHz (Fig. 2). This will, however, produce no difference in spectral index between these two frequencies. The 15-GHz data have not been compared, because LP have subtracted the core emission, which may contribute a large fraction of the total flux at such a high frequency. We believe that the 15-GHz flux scale agrees with that of LP to within 5 per cent, leading to an error in spectral index between 5 and 15 GHz of less than ± 0.04. These systematic errors affect all strips equally, thus the relative changes in spectral index across a lobe should be more accurate than the absolute values.

(iii) The application of a flux cut-off. The 3σ cut-off applied at all the frequencies will lead to an underestimate of

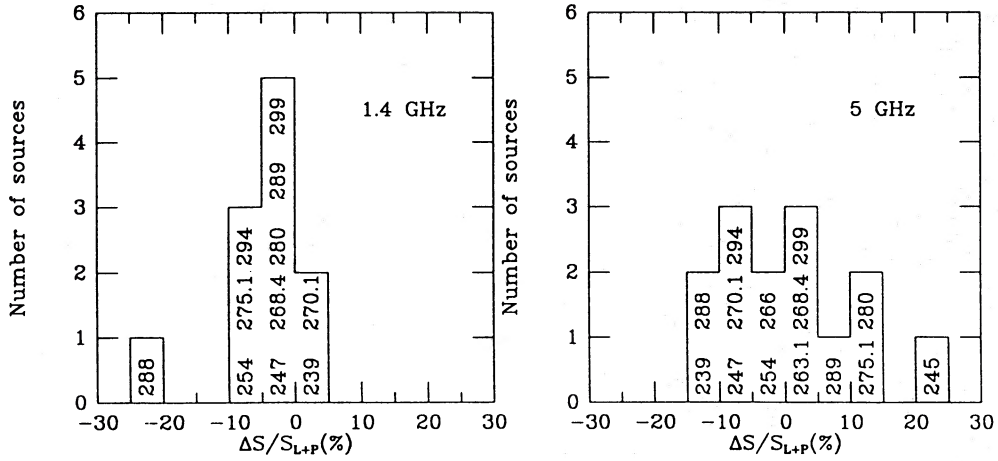

Figure 2. Histograms showing the difference between the flux-density scales of our measurements and those of LP.

the flux at higher frequencies, giving an overestimate of the spectral index. Generally this effect is small. Take 3C289 for example: Fig. 15(a) shows maps of 3C289 at 1.4 and 5 GHz, with the strips being marked on the 1.4-GHz map. Strip OX_1 is in one of the faintest parts of the source and its spectrum is therefore likely to be most affected by the cut-offs. The integrated flux density at 5 GHz of this strip with a 3σ cut-off is 7.80 mJy, whilst with no cut-off it is 7.93 mJy. This leads to a difference in spectral index between 1.4 and 5 GHz of only 0.013.

4.3 Spectral ageing analysis

The spectral age, the time which has elapsed since the electrons were last accelerated, can be derived from the steepening in the radio spectrum due to synchrotron and inverse-Compton losses.

Assuming that: (i) the magnetic flux density of the source (B) is constant throughout the process; (ii) initially the electrons are injected with a constant power-law energy spectrum having injection index γ, $N(E)\,dE = N_0 E^{-\gamma} dE$, and (iii) the electrons are isotropized on time-scales short compared with their radiation lifetime (Jaffé & Perola 1973), the electron age is given by

$$t = \left[\frac{9C_1 B}{4C_2^2 (B^2 + B_{\rm MWB}^2)^2 \nu_{\rm T}}\right]^{1/2}$$

$$\simeq 5.02\,\frac{(B/{\rm nT})^{1/2}}{(B/{\rm nT})^2 + (B_{\rm MWB}/{\rm nT})^2}\,(\nu_{\rm T}/{\rm GHz})^{-1/2} 10^7\,{\rm yr}, \qquad (1)$$

where C_1 and C_2 are constants defined by Pacholczyk (1970). $B_{\rm MWB} = 0.32(1+z)^2$ nT and is the equivalent magnetic field strength of the microwave background radiation, included in equation (1) to allow for inverse-Compton losses. $\nu_{\rm T}$ is the break frequency below which the spectrum tends to be a power law with spectral index $\alpha_0 = (\gamma - 1)/2$ and above which the integrated spectrum steepens.

The break frequency is derived by fitting a theoretical spectrum to the observed one, assuming that the initial (injection) spectral index α_0 is equal to the low-frequency spectral index for the whole source derived from the data of LP between 38 MHz and 1 GHz. None of the sources here shows significant low-frequency turnover in this range.

To demonstrate the goodness of the fits to the model spectra, Fig. 3 shows the three-point spectrum of each strip across 3C289 (as indicated in Fig. 15a) fitted with a theoretical synchrotron-loss spectrum with an injection index, γ, of 2.4. It is seen that in most strips the observed spectra fit the theoretical ones well, apart from those strips close to the galaxy where the core emission is dominant. The data are consistent with a model in which the injection index is constant in time.

The true magnetic field strength remains one of the greatest uncertainties in this spectral ageing calculation. We have assumed a constant magnetic field throughout the source, and, to minimize the effect of adiabatic expansion, we use the magnetic flux density just outside the hotspot region, as discussed by Alexander (1987). The field is calculated from equipartition arguments (e.g. Miley 1980; AL), by assuming equality in the energy of protons and electrons, a filling factor of unity, a radio spectrum ranging from 10 MHz to 100 GHz, and cylindrical symmetry. The resultant equipartition magnetic flux densities ($B_{\rm eq}$) are listed in Table 4. Also listed are the values of $B_{\rm MWB}$ for these sources. On average, the source magnetic field is 4–5 times $B_{\rm MWB}$. Once $B_{\rm eq}$ and $\nu_{\rm T}$ are determined, the synchrotron age can be deduced from equation (1).

5 RESULTS

The results for each source are presented in Figs 4–17. Each figure contains the following information (for further details, see the caption to Fig. 4).

(a) Total intensity maps. The frequency is indicated at the top of each map. For sources which have two sets of resolutions, both sets of maps are shown.

(b) Strip profiles of total intensity along each lobe at the lowest frequency available, and the spectral index and spectral age along the lobes. The origins of the profiles are arbitrary.

The maps of spectral index, presented as grey-scales, are shown in Liu & Pooley (1991a).

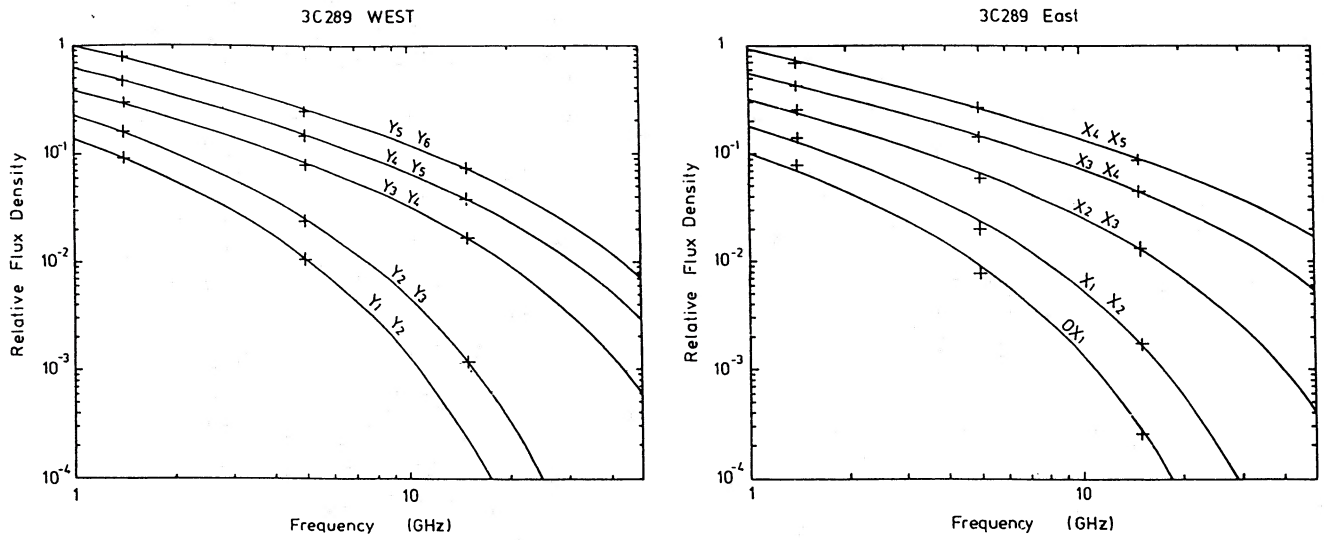

Figure 3. Spectra fits in 3C289. Each spectrum corresponds to one of the strips shown in Fig. 15(a). Note the good fit and the increasing curvature of the spectra with distance away from the hotspot.

Table 4. The results.

Source	α_0	B_{mwb}	B_{eq}(nT)		v_{lobe}(c)		α^{peak}		x-lobe
		(nT)	x-lobe	y-lobe	x-lobe	y-lobe	x-lobe	y-lobe	
3C239	0.90	2.48	8.0±0.5	5.5±0.5	0.10±0.03	0.13±0.02	1.11	1.04	Nf
3C245	0.78	1.31	-	11.2±0.2	-	0.18±0.04	-	0.96	W
3C247	0.70	0.97	4.5±0.1	4.6±0.2	0.13±0.01	0.10±0.02	0.84	0.80	Nf
3C254	0.80	0.96	4.5±0.1	4.6±0.1	0.10±0.02	0.13±0.02	1.04	0.85	E
3C263.1	0.65	0.59	13.0±1.0	11.0±1.0	0.26±0.10	0.18±0.04	1.60	0.78	Nf
3C266	0.80	1.64	11.8±0.5	12.5±0.2	0.16±0.04	0.20±0.04	1.53	1.29	N
3C268.4	0.80	1.83	5.0±0.2	5.0±0.3	0.24±0.04	0.15±0.03	1.11	0.86	Nf
3C270.1	0.75	2.02	5.8±0.4	7.7±0.3	0.18±0.03	0.15±0.03	1.10	0.86	Np
3C275.1	0.70	0.77	3.3±0.1	4.0±0.2	0.10±0.02	0.11±0.03	0.73	0.96	N
3C280	0.70	1.27	4.5±0.5	6.0±0.5	0.12±0.02	0.13±0.02	0.98	0.66	E
3C288	0.80	0.49	2.1±0.1	2.1±0.1	0.05±0.01	0.06±0.02	0.87	0.77	N
3C289	0.70	1.23	4.8±0.2	4.2±0.3	0.10±0.02	0.09±0.02	0.84	0.91	Sf
3C294	1.00	2.46	6.0±0.4	4.0±0.1	0.14±0.03	0.18±0.03	1.10	1.28	Nf
3C299	0.70	0.59	5.5±0.5	2.8±0.1	0.21±0.05	0.03 ±0.01	0.93	0.74	Nf

In general, electrons close to the hotspots appear younger than those further away. The synchrotron lifetimes are generally less than 3×10^6 yr, younger than those of the low-power sources of AL (5×10^7 yr).

Straight-line fits to the plots of age versus hotspot distance for each lobe gives a characteristic speed, $v_{\rm lobe}$, the speed separating the hotspot from the lobe material. The straight-line fits might be expected to go through $t = 0$ at the hotspots, the hotspot being the point at which particle acceleration is now occurring. However, no source shows zero age at the hotspot, and all of the sources for which we have three-frequency spectra at the hotspots show curvature (Liu & Pooley 1991a). Possible explanations include: (i) the hotspots have all been inactive for times ranging between 10^5 and 10^6 yr; (ii) the spectra of the hotspots are contaminated by emission from the lobe material, or (iii) the magnetic fields in the hotspots themselves are substantially stronger than those in the more extended regions. We regard the first possibility as improbable, while (ii) is certainly the case with the current data, where the resolution corresponds to a linear scale of the order of several kiloparsec. Alexander (1987) argued for (iii) in his study of 3C234.

5.1 Notes on individual sources

3C239. In the low-resolution 1.4-GHz map of this source (Fig. 4a) there is some radio emission at the 2.5σ level coincident with the position of the associated galaxy; since it is not visible on the 5- and 15-GHz maps, it is unlikely to be core emission. The hotspot in the eastern component is at one

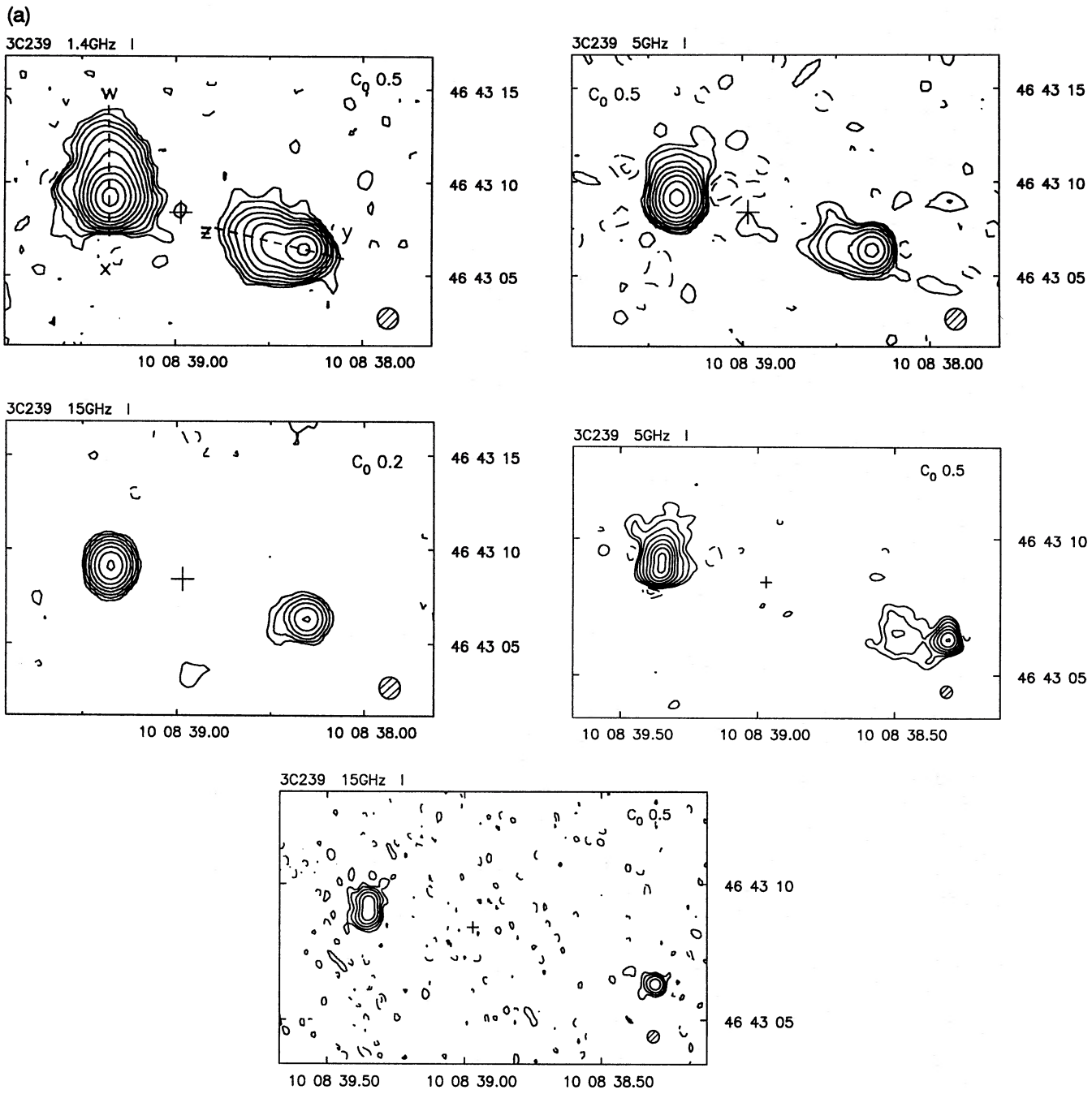

Figure 4. (a) Total intensity maps for 3C239. The frequency is indicated at the top of the map. The contours are logarithmic, separated by a factor of 2. The level of the bottom contour in mJy is shown by C_0. Negative contours are dashed. The crosses mark the position of the optical identifications. The hatched circles indicate the half-power beamwidth. The letters on the first map indicate the axes along which the spectra are determined. (b) Strip profiles of total intensity at 1.4 GHz and the spectral index and age along the lobe axes indicated by the letters shown in (a). The bar and the number below it mark the half-power beamwidth. The number shown on the age–distance plot is the initial spectral index.

side of the lobe, which is itself extended perpendicular to the source axis. The spectra are flatter at both hotspots, and gradually steepen along the lobes. In the eastern lobe, the spectrum steepens away from the hotspot in a direction nearly perpendicular to the source axis.

3C245. This source has a strong core, a one-sided jet pointing at the bright western component and a more extended and weaker eastern component. The ratio of the peak brightnesses of the two components is 13, though the total flux densities of the two differ by only a factor of 2. At 15 GHz, the core and the western lobe are still visible, but the surface brightness of the eastern component is very low. This source is identified with a quasar; the radio core is moderately superluminal (Hough & Readhead 1989; Foley & Barthel 1990). The spectral index of the core between 5 and 15 GHz is ~0.45. Earlier low-frequency observations

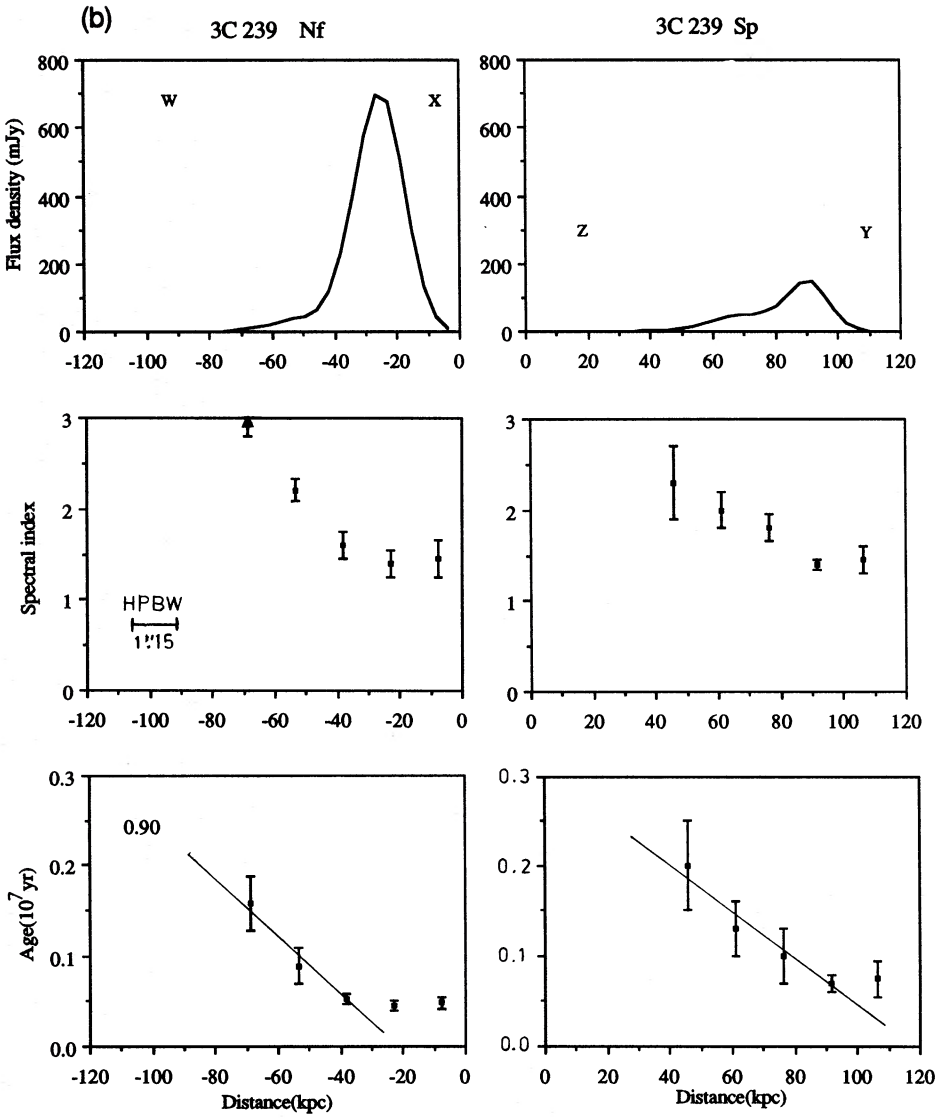

Figure 4 – *continued*

(e.g. Harris 1974; Davis, Stannard & Conway 1983) suggest that the core becomes self-absorbed below ~ 250 MHz. The spectral index distribution between the core and the western component shows two main features: a steepening along the jet away from the core which may be due to the combination of a flat-spectrum jet and steep-spectrum lobe, and a steepening away from the hotspot towards the core. The velocity derived from the latter is the lobe–hotspot separation speed. The eastern lobe clearly has a steep spectrum ($\alpha_{15}^{5} \sim 1.2$), but it is too faint and diffuse to make any sensible estimates of its spectral age.

3C247. The radio structure of 3C247 shows signs of an X-shaped structure. A core of 3.5 mJy at 5 GHz, also detected by Laing & Riley (private communication), lies 1.5 arcsec south-west of the optical identification – the difference between the radio and optical positions is not significant. Liu & Pooley (1991b) discuss the [O II] line-emission gas, which is associated with the galaxy and is extended along the radio source. The spatial coincidence suggests a connection between the presence of the dense ionized gas and the distorted shape of the radio source. The continuous spectral steepening along the distorted arms XW and YZ is consistent with the idea that the faint emission in regions W and Z is backflow from the hotspots X and Y respectively.

3C254. The associated quasar, which has a radio core of 19 mJy at 5 GHz (Owen & Puschell 1984), is very close to the eastern hotspot. The eastern component is extended roughly perpendicular to the source axis – a 'side-flow' similar to that in the eastern lobe of 3C239. The spectrum steepens along this side-flow, giving a lobe–hotspot separation speed of $0.13c$. The western component shows the classic backflow features with the spectrum steepening towards the quasar.

3C263.1. This source has a fairly bright core (3.2 mJy at 5 GHz). The Sp hotspot is double, with the more compact hotspot lying closer to the nucleus. The brighter part of the Nf lobe extends southwards rather than towards the nucleus. The spectra in the double-hotspot region steepen from the more compact hotspot to the more diffuse one; the speed was derived purely from this steepening. There is no 15-GHz information available on the diffuse emission in the south.

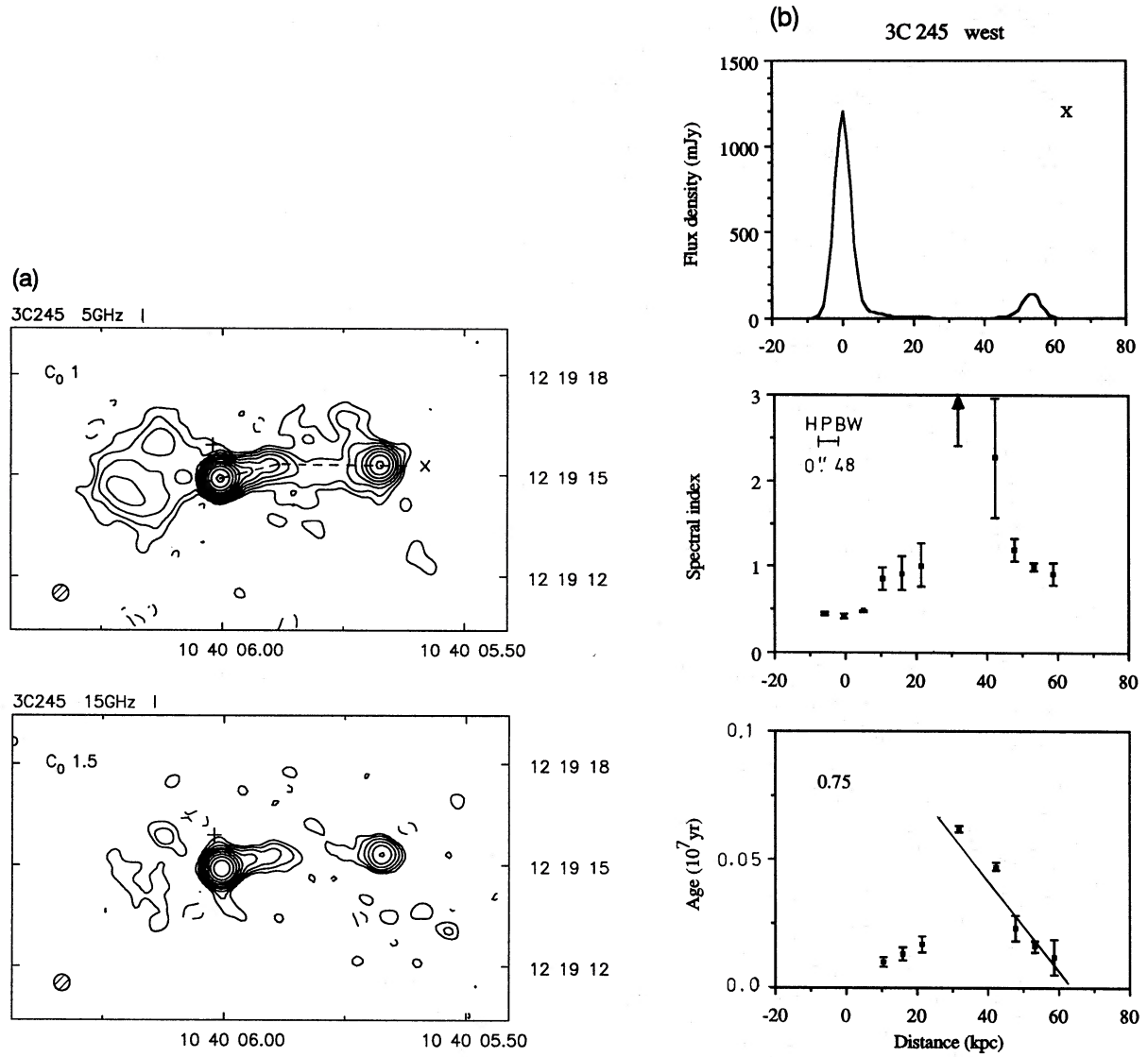

Figure 5. (a) Total intensity maps and (b) strip profiles of total intensity at 5 GHz, spectral index and age along the lobe axes indicated by the letters in (a), for 3C245. See the caption to Fig. 4 for further details.

The spectral index (between 5 and 15 GHz) of the Nf hotspot is higher by 0.8 than that of the more compact of the two Sp hotspots.

3C266. There is a possible 0.4-mJy core at the centre of the source on the 5-GHz map, but it could not be confirmed by the rather noisy 15-GHz map. Both hotspots in this source lie on the axis some way behind the leading edges of the lobes. The spectra are flatter at these embedded hotspots, steepening both outwards and inwards with about the same gradient.

3C268.4. The high-resolution maps show a jet-like feature pointing from the strong core of this quasar towards the more compact one of the double hotspots in the Sp lobe. The spectral indices are derived from the lower resolution maps. The spectrum in the Sp lobe steepens along the extended emission towards the south-west. Like 3C263.1, 3C268.4 has one hotspot (the Nf one) with a much steeper spectrum than the other. The core has a spectral index of 0.3 between 1.4 and 5 GHz.

3C270.1. This radio source is associated with a quasar, coincident with a strong radio core (190 mJy at 5 GHz). A knot lying between the core and the southern lobe (see the 5-GHz high-resolution map) indicates the presence of a jet. The southern hotspot lies off the axis of the lobe, but not at the outer edge. All these features are confirmed by the 5-GHz VLA map at a similar resolution of Stocke, Burns & Christiansen (1985, SBC). Emission in the S component extends from the hotspot both outwards and back towards the nucleus. The separation between the hotspot and the backflow only is considered.

3C275.1. This source is associated with a quasar. High-resolution observations by SBC and Laing (1988) show a jet pointing towards the north-west hotspot. On the spectral index map presented by Liu & Pooley (1991a) it can be seen that the spectrum is almost unchanged along the jet path between the core and the Np hotspot. The integrated strip spectra still steepen, however, although not as significantly as those in the S lobe, from the hotspot back towards the

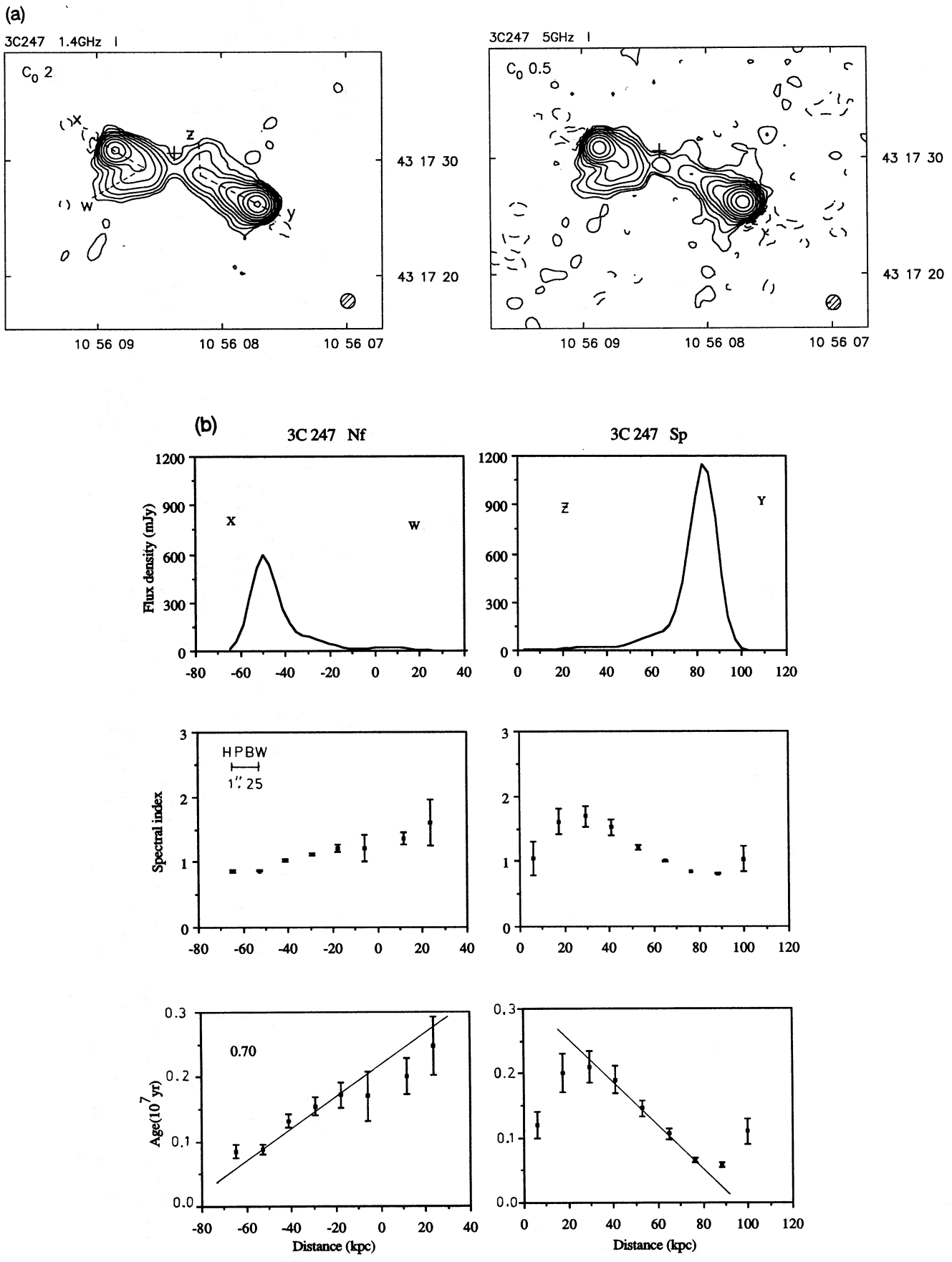

Figure 6. (a) Total intensity maps and (b) strip profiles of total intensity at 1.4 GHz, spectral index and age along the lobe axes indicated by the letters in (a), for 3C247. See the caption to Fig. 4 for further details.

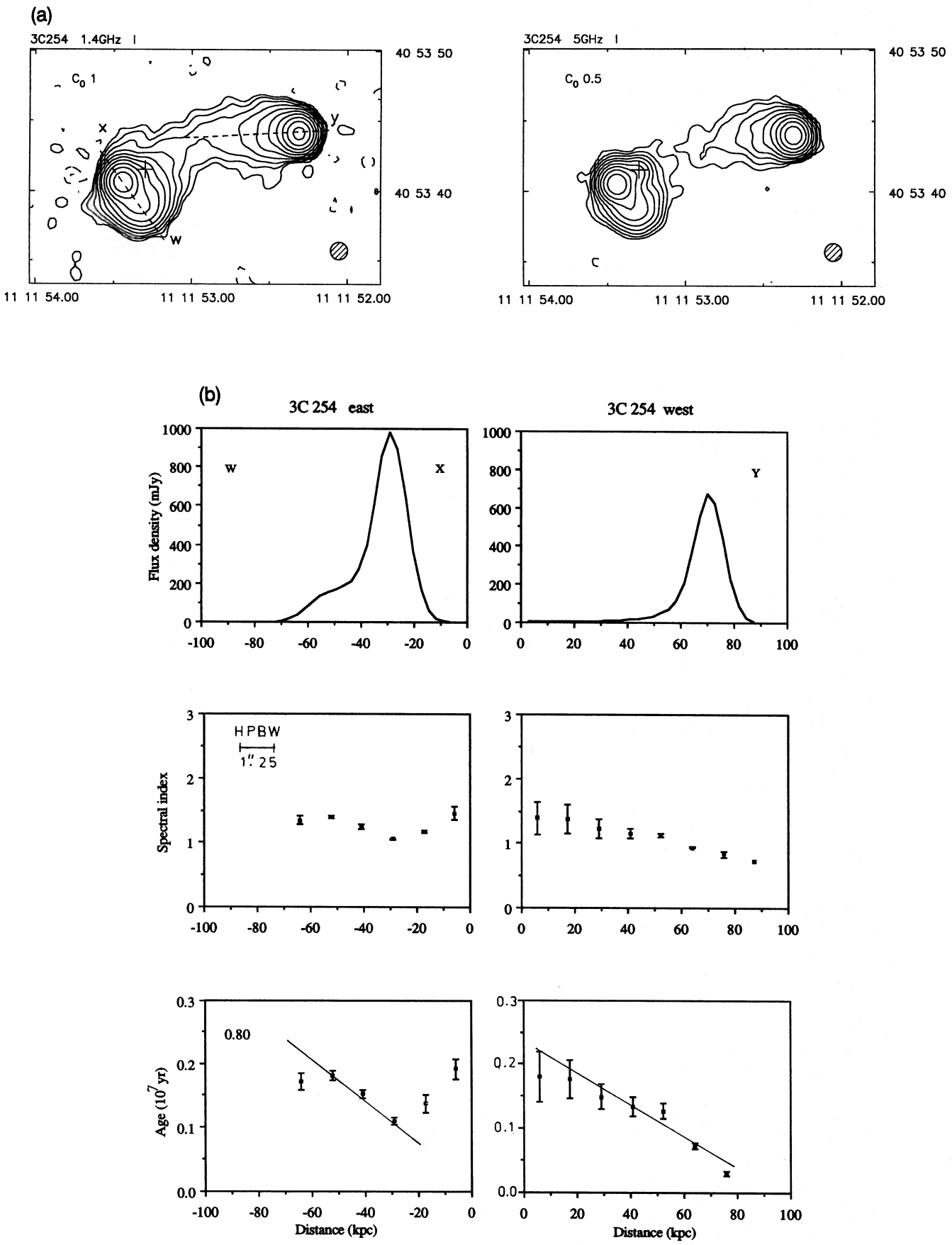

Figure 7. (a) Total intensity maps and (b) strip profiles of total intensity at 1.4 GHz, spectral index and age along the lobe axes indicated by the letters in (a), for 3C254. See the caption to Fig. 4 for further details.

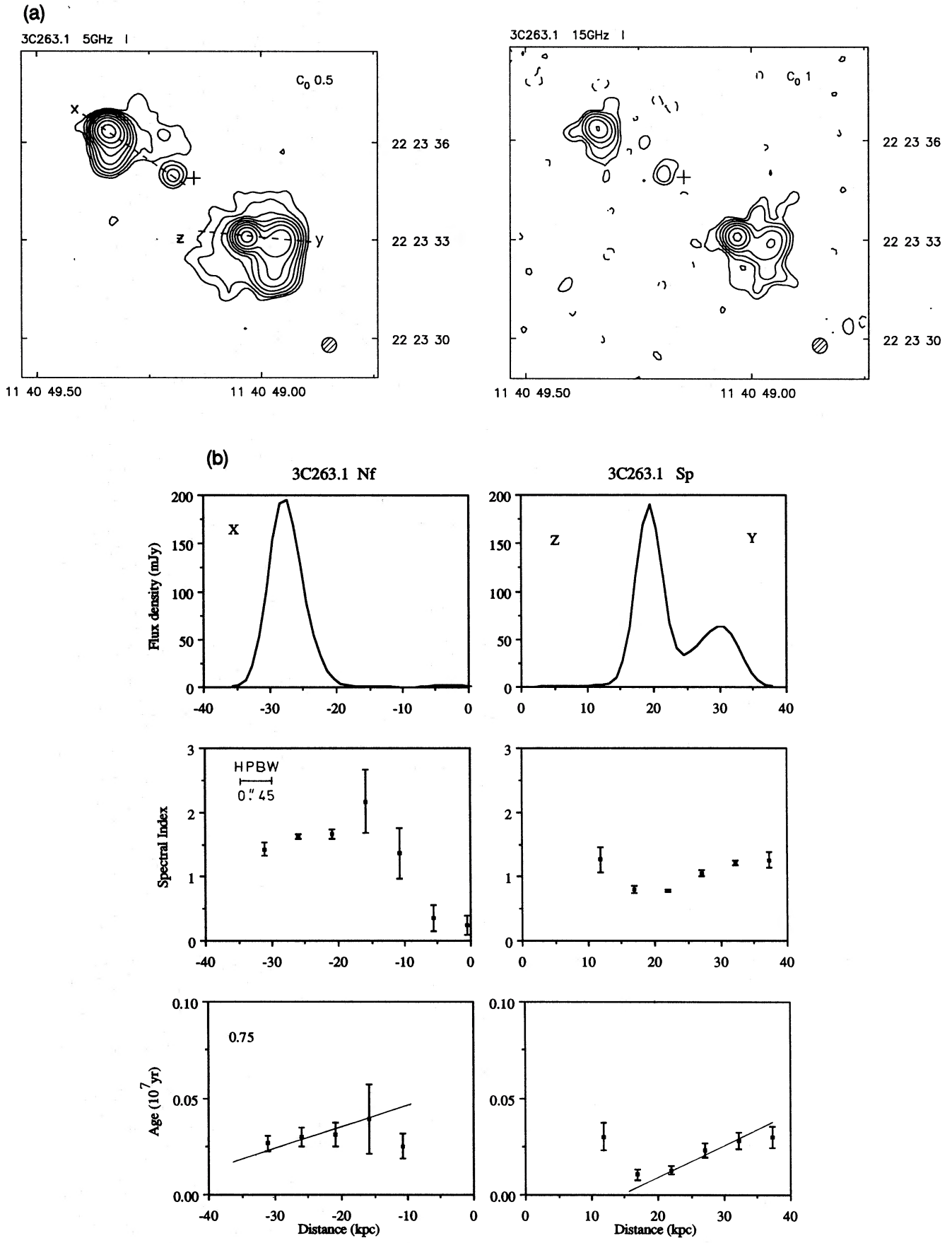

Figure 8. (a) Total intensity maps and (b) strip profiles of total intensity at 5 GHz, spectral index and age along the lobe axes indicated by the letters in (a), for 3C263.1. See the caption to Fig. 4 for further details.

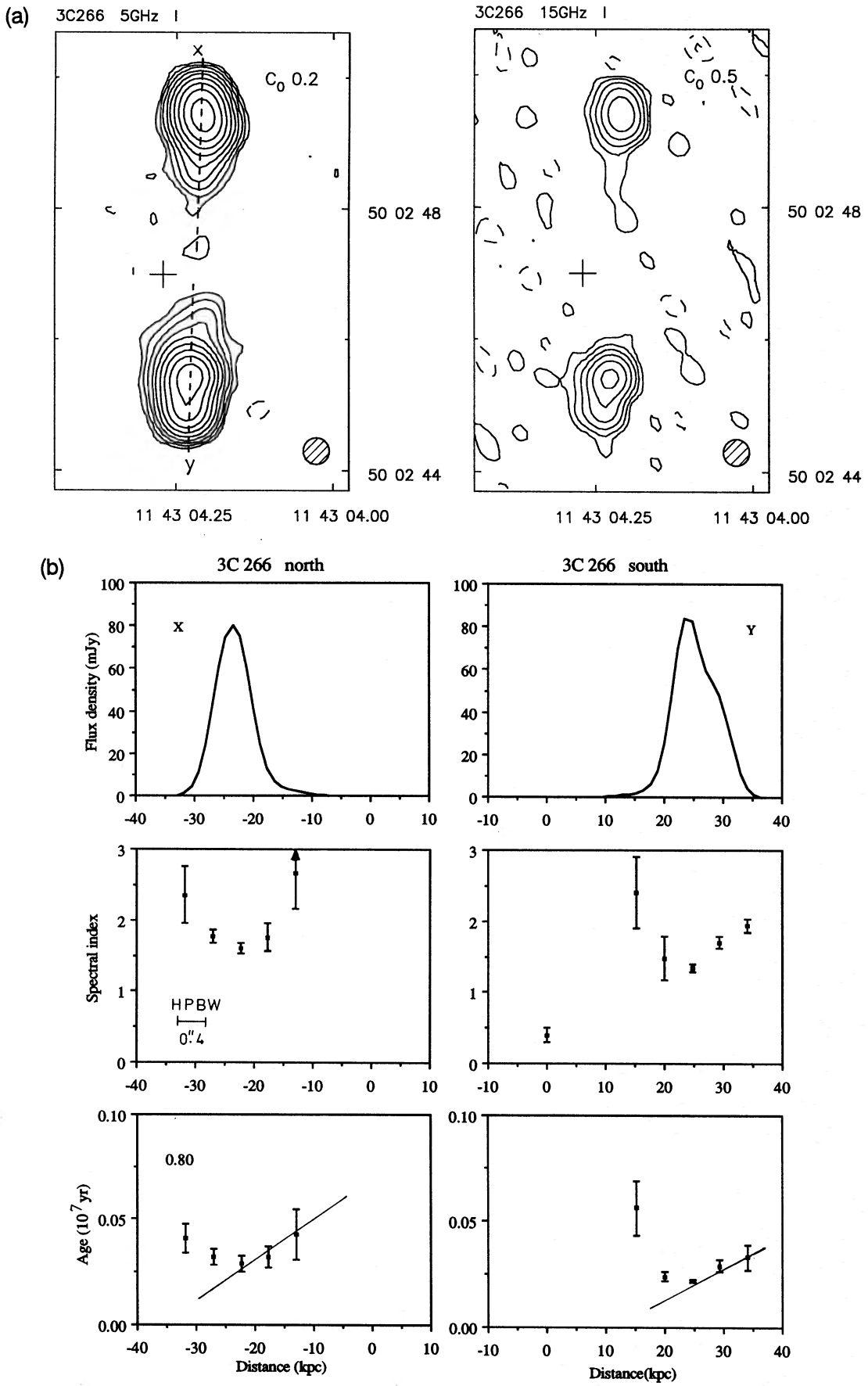

Figure 9. (a) Total intensity maps and (b) strip profiles of total intensity at 5 GHz, spectral index and age along the lobe axes indicated by the letters in (a), for 3C266. See the caption to Fig. 4 for further details.

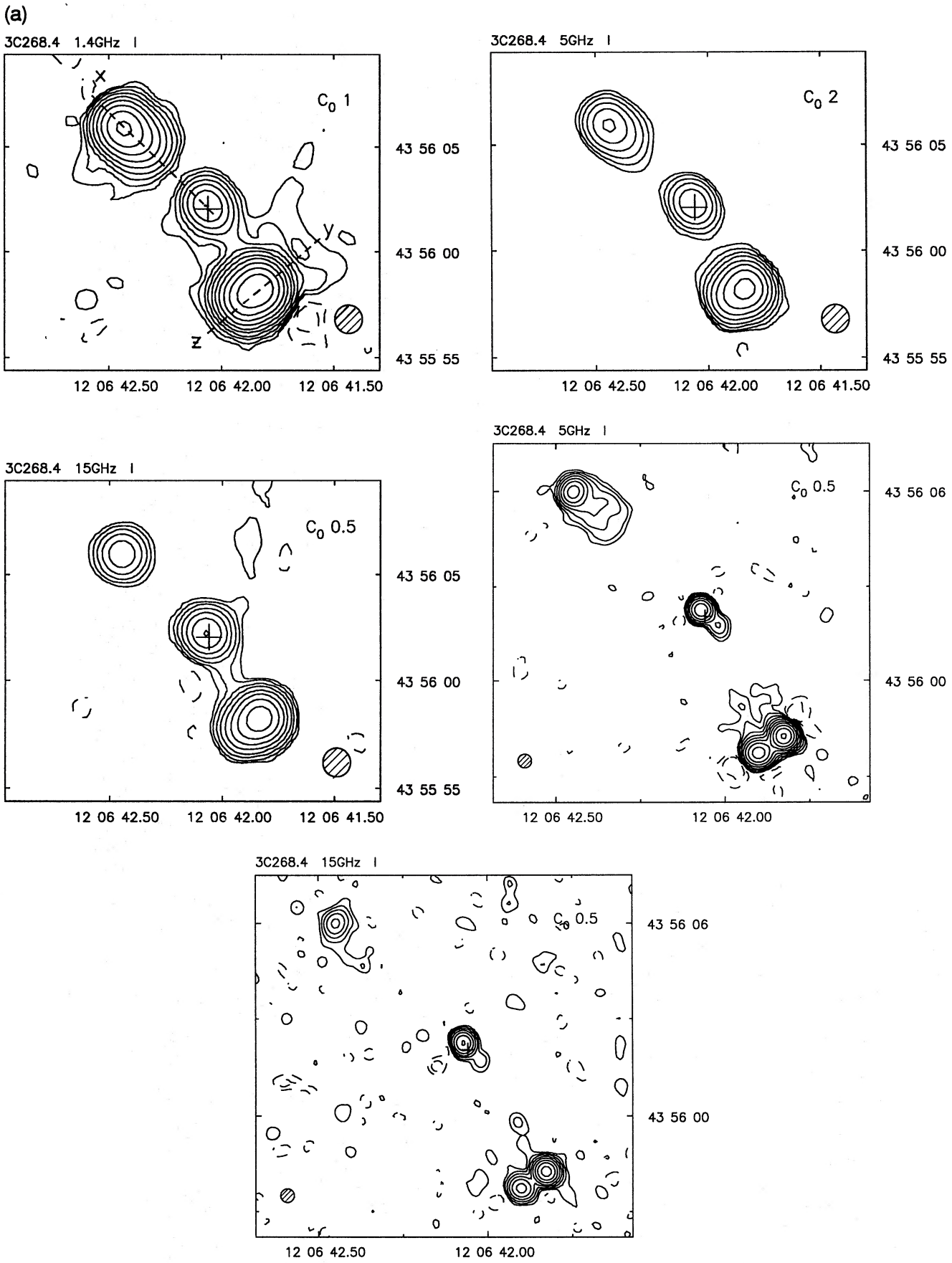

Figure 10. (a) Total intensity maps and (b) strip profiles of total intensity at 1.4 GHz, spectral index and age along the lobe axes indicated by the letters in (a), for 3C268.4. See the caption to Fig. 4 for further details.

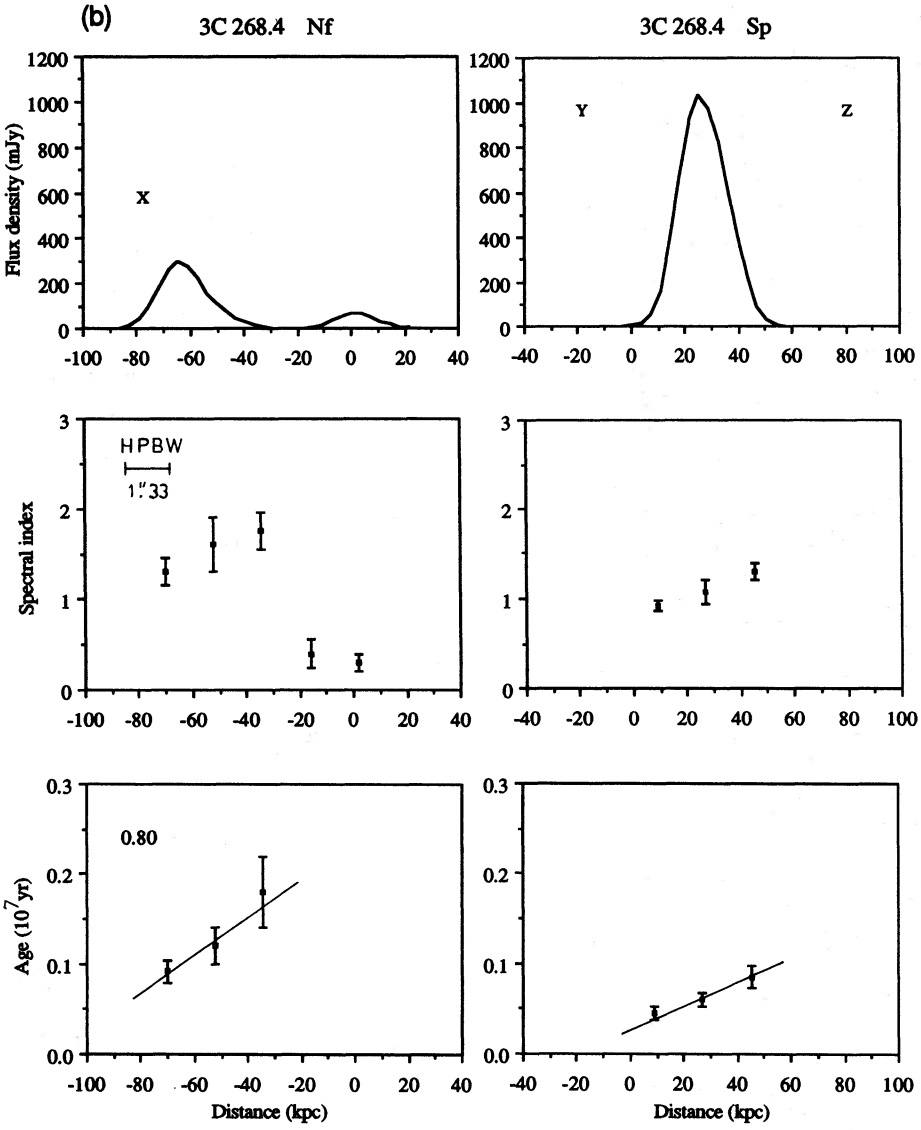

Figure 10 – *continued*

nucleus. This indicates that the bright jet does not contribute a significant amount of flux to the total. The integrated spectrum of the whole source is straight from 80 MHz to 5 GHz with a spectral index of 0.9 (data from LP), agreeing with our current observation that there is not much steepening in the spectrum between 1.4 and 5 GHz across this source. A companion galaxy next to the S hotspot and lying along the Nf hotspot–core axis was observed by Hintzen (1984). Liu & Pooley (1990) found strong depolarization associated with the region where the companion galaxy lies, in agreement with the suggestion by SBC that the distortions in the S component are the result of an interaction between the quasar itself and the companion galaxy.

3C280. Neither hotspot lies at the outer extremities of the source. The west hotspot lies at the SW edge of the lobe, the diffuse lobe emission extending both back towards the nucleus and northwards. The E lobe is less extended with the hotspot embedded in the middle. There is a core with ~2 mJy at 5 GHz and $\alpha_5^{1.4} \sim 0.5$. The spectra are flatter at the hotspots and steepen along the extended emission; in the W lobe steepening occurs both back towards the nucleus and northwards, following the extension of the lobe emission.

3C288. The edge-darkened structure and spectral index distribution make 3C288 look like a distorted FRI radio tail source, though its luminosity ($10^{26.7}$ W Hz^{-1} sr^{-1}) is much higher than that for a normal tailed source. There is a jet and a counter-jet near the radio core (Bridle *et al.* 1989) with faint 'wings' of emission connected to the elongated lobes. The slightly brighter features in the lobes, which lie on the line of the jet and counter-jet, might be the hotspots, but the peak in the northern component has a steeper spectrum than its surroundings. The host galaxy is believed to be the dominant member of a distant cluster (Wyndham 1966); consequently the peculiar structure of 3C288 is unlikely to be caused by the motion of the galaxy through the intracluster medium (ICM). The spectra steepen smoothly from east to west in both the N and S components. Our spectral ageing results are consistent with those of Bridle *et al.* (1989).

3C289. Its remarkably linear, symmetric classical-double

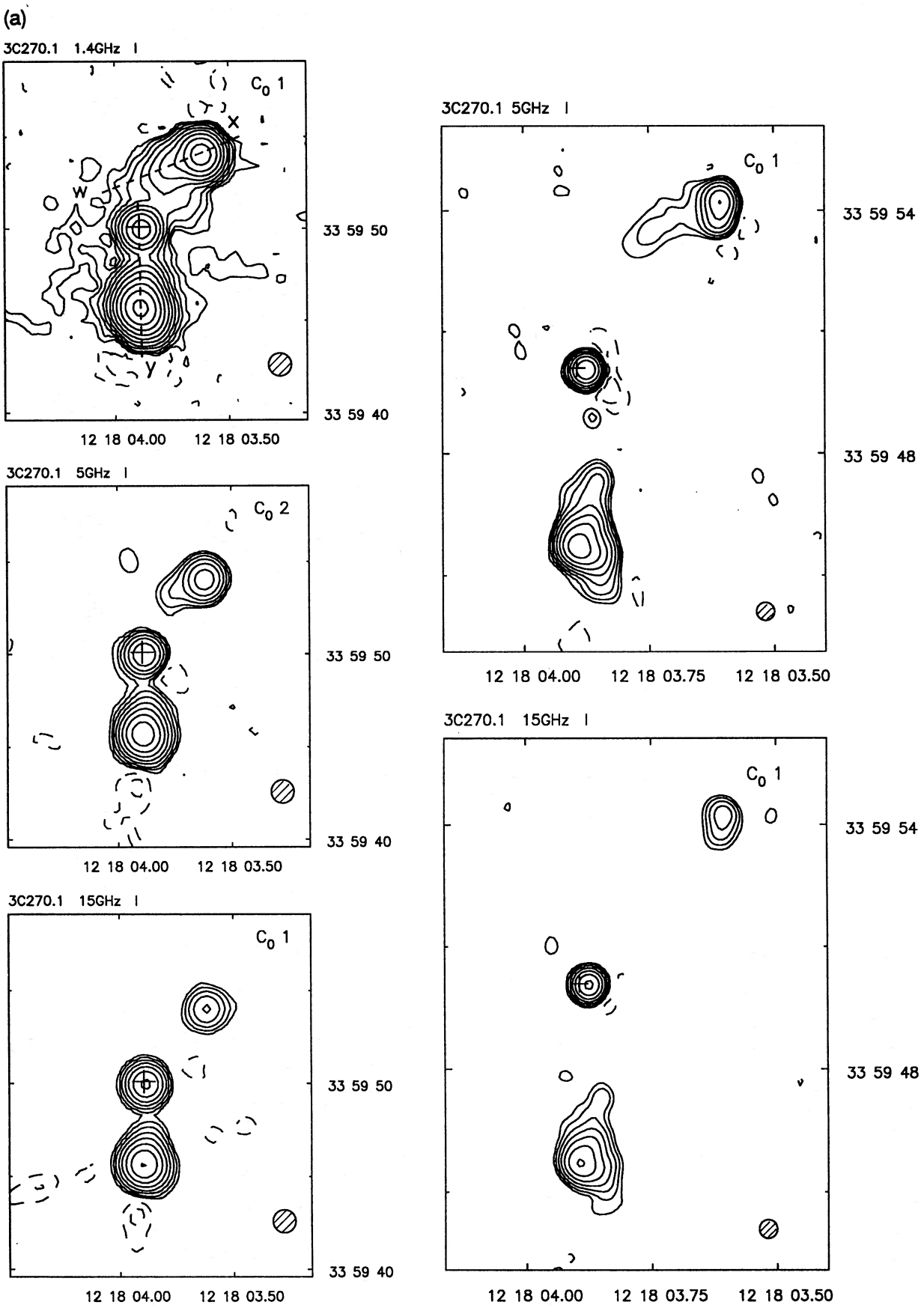

Figure 11. (a) Total intensity maps and (b) strip profiles of total intensity at 1.4 GHz, spectral index and age along the lobe axes indicated by the letters in (a), for 3C270.1. See the caption to Fig. 4 for further details.

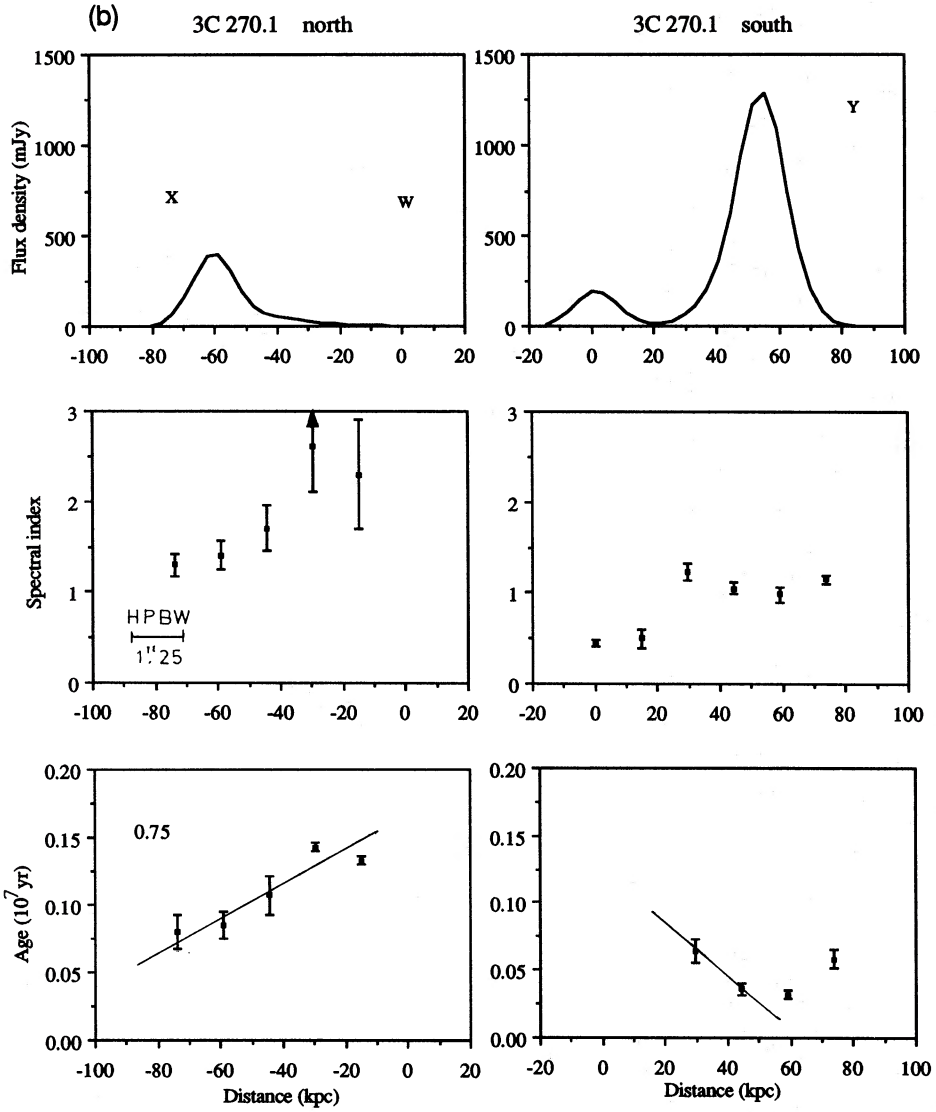

Figure 11 – *continued*

structure makes this source unusual among these high-luminosity objects. The hotspots lie at the outer edges of the lobes, and there is spectral steepening towards the nucleus in both lobes. Around the nucleus the spectrum becomes flatter again where the core emission dominates.

3C294. This source is identified with an object with the optical spectrum of a galaxy, though the optical image is almost obscured by a bright star in the field. The northern hotspot is embedded in a diffuse low-brightness lobe, and the spectrum steepens both back towards the nucleus and outwards. The backflow may be slightly faster than the outflow, but the difference is not very significant. High-resolution images of the source show clearly a 'precessing jet' structure (McCarthy *et al.* 1990). Even in our moderate-resolution map, a flat-spectrum knot [A in Fig. 16(a) and fig. 2 in Liu & Pooley 1991a] indicates a possible change in the jet direction.

3C299. Two components are visible on the low-resolution maps of this source, the south-western lobe (Y) and the brighter component X. Component X is noted by Riley & Pooley (1975) as being coincident with the probable identification. They postulated that there might be a faint lobe north-east of the source below the sensitivity of their observation. Such a lobe is not visible in the current observations with high dynamic range. Indeed, our high-resolution observations show a core (~ 1 mJy at 5 GHz, marked A in Fig. 17a) lying on the source axis about 3 arcsec from component X. We believe that the component A is coincident with the identification and the brighter component X is the Nf lobe of this double source. The source is thus highly asymmetrical with respect to the position of the identification, like 3C254.

There are two galaxies between the brighter component X and the core A. The position listed by Riley & Pooley and marked as a cross on the maps is the average position of the two galaxies. The radio core is within the uncertainty of the position given by Riley & Pooley.

The Nf component appears compact in the low-resolution observations and shows little variation in spectral index across it, leading to a high velocity, $0.2c$.

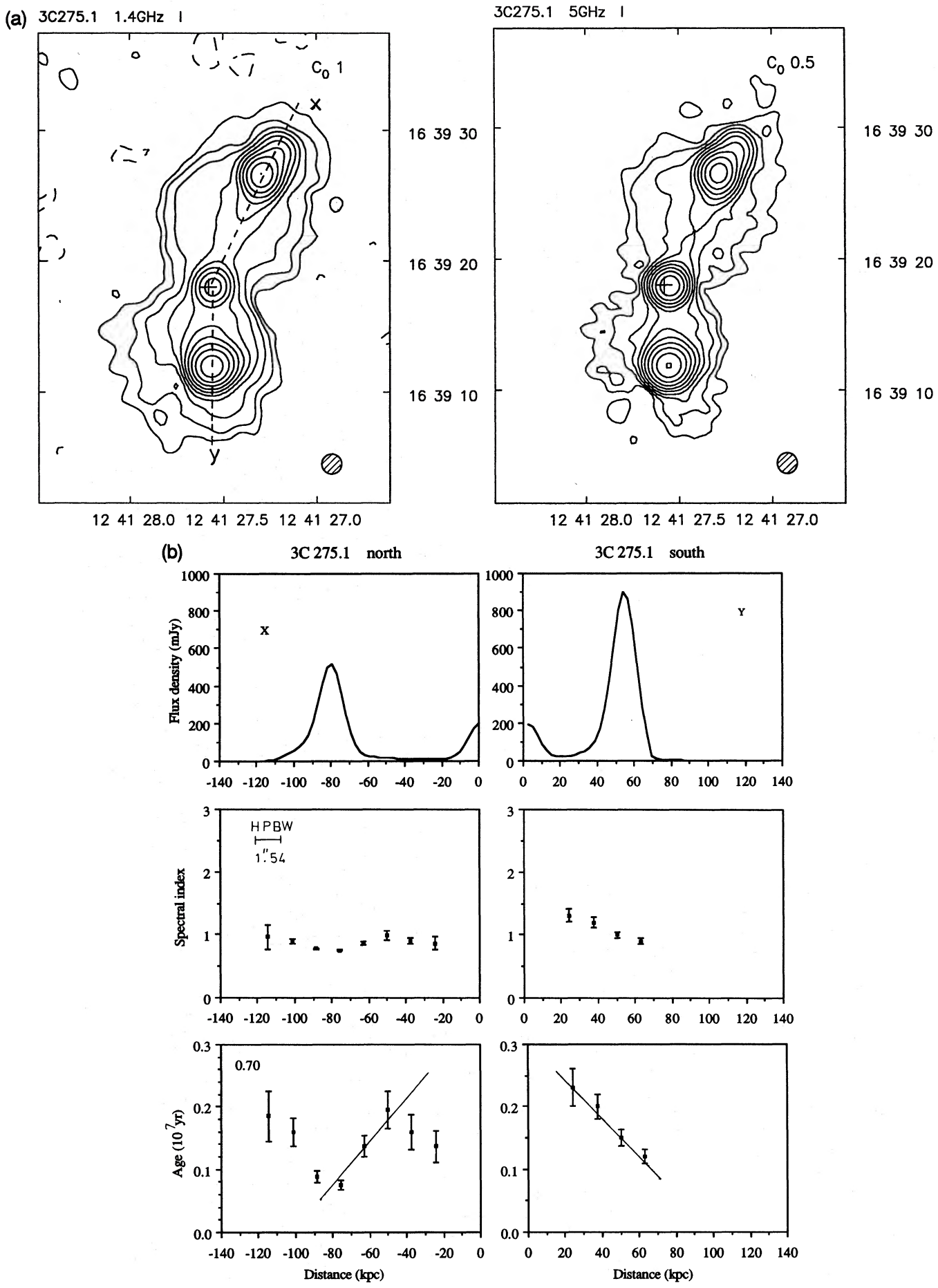

Figure 12. (a) Total intensity maps and (b) strip profiles of total intensity at 1.4 GHz, spectral index and age along the lobe axes indicated by the letters in (a), for 3C275.1. See the caption to Fig. 4 for further details.

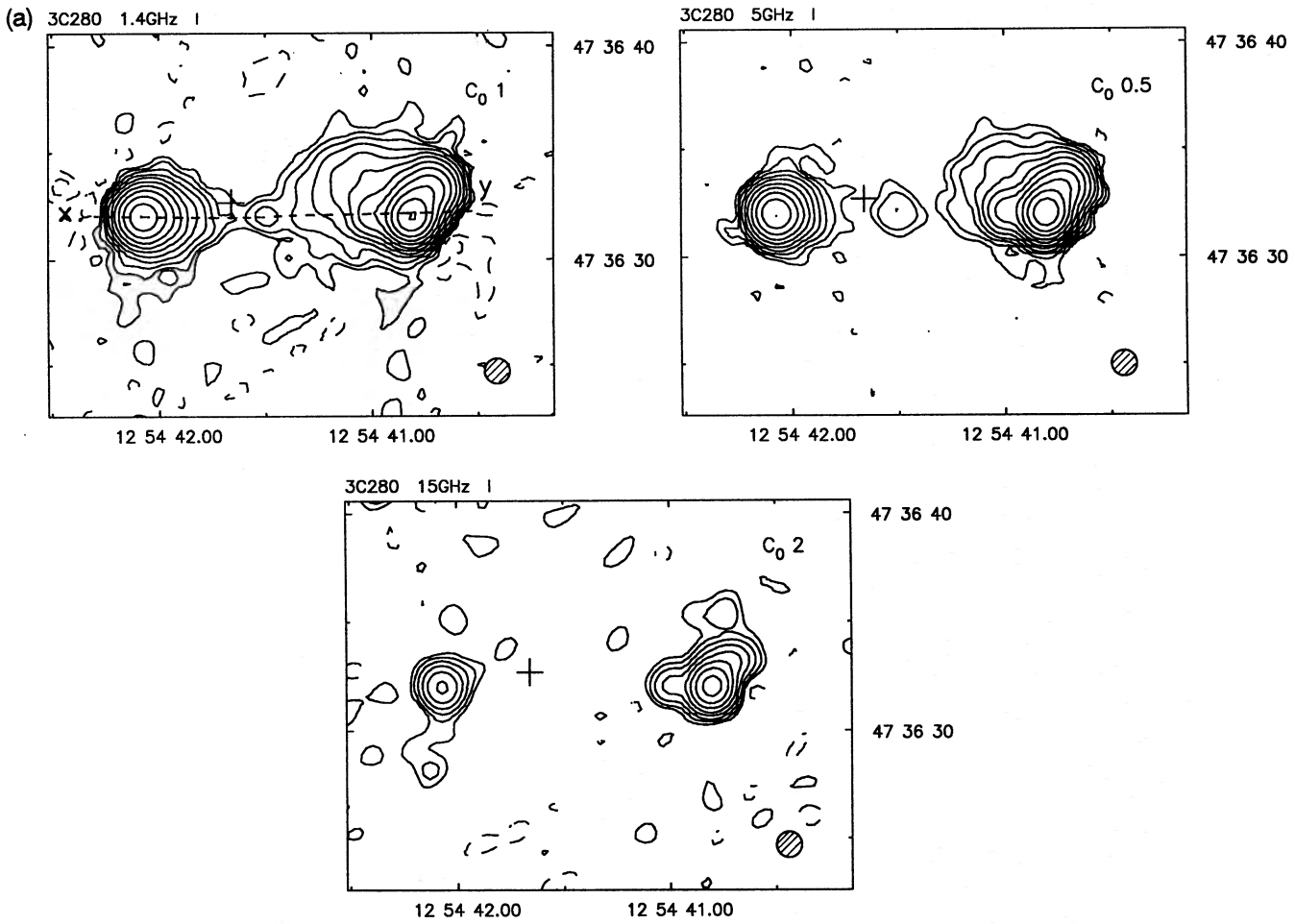

Figure 13. (a) Total intensity maps and (b) strip profiles of total intensity at 1.4 GHz, spectral index and age along the lobe axes indicated by the letters in (a), for 3C280. See the caption to Fig. 4 for further details.

6 DISCUSSION

6.1 Structures and spectra

One of the most significant differences between the sources at low and high power in the whole sample is the different structures of the lobes. Most of the relatively low-power sources in the AL sample resemble the simple picture of FRII sources, with the hotspots sitting at the outer edges of the lobes and with the extended lobe emission connecting the hotspots to the nucleus. Most of the small and high-luminosity sources discussed here, however, do not show the textbook FRII structure. There is a variety of distortions seen in these high-power objects, such as the sharp bends in 3C270.1 and 275.1, the double-hotspots in 3C263.1 and 268.4, and the X-shape of 3C247. Hotspots are embedded in the middle of the lobe in 3C266, 280 and 294, with diffuse emission extending away from as well as back towards the nucleus. The eastern lobes of 3C239 and 254 extend roughly at right angles to the source axes. We frequently find that the two lobes in a source have rather different types of structure, often in the sense that one lobe extends towards the nucleus and one does not. Similar structures are observed by Barthel & Miley (1988), who analyse a large number of quasars with $z > 1.5$ and show that the distant quasars have a more bent, distorted appearance than those nearby. They suggest that this is due to an interaction of the radio source with an epoch-dependent interstellar or intracluster medium. SBC and Liu & Pooley (1990) show that the bent quasar 3C275.1 is a result of interaction between the radio ejecta of the quasar and a companion galaxy. Strong evidence for the distorted structures being caused by the interaction of radio sources with gas clouds is provided by extranuclear line-emitting gas associated with powerful radio galaxies (e.g. McCarthy *et al.* 1987, 1990; Liu & Pooley 1991b).

Nevertheless, the hotspots always exhibit the flattest spectra and thus have the youngest population of electrons, and the apparent ages increase away from the hotspots into the lobe emission, regardless of the direction in which the lobe emission extends. The velocity derived from such a steepening represents, in the classic FRII lobes, a combination of the hotspot advance speed and the backflow velocity of the material flowing out of the hotspot. In the distorted lobes the derived separation speed must represent only the speed of the post-shock material flowing out of the hotspot.

Those lobes showing classic backflows, such as the western components of 3C239, 247 and 254, and both the lobes of 3C289, do not have significantly different spectral

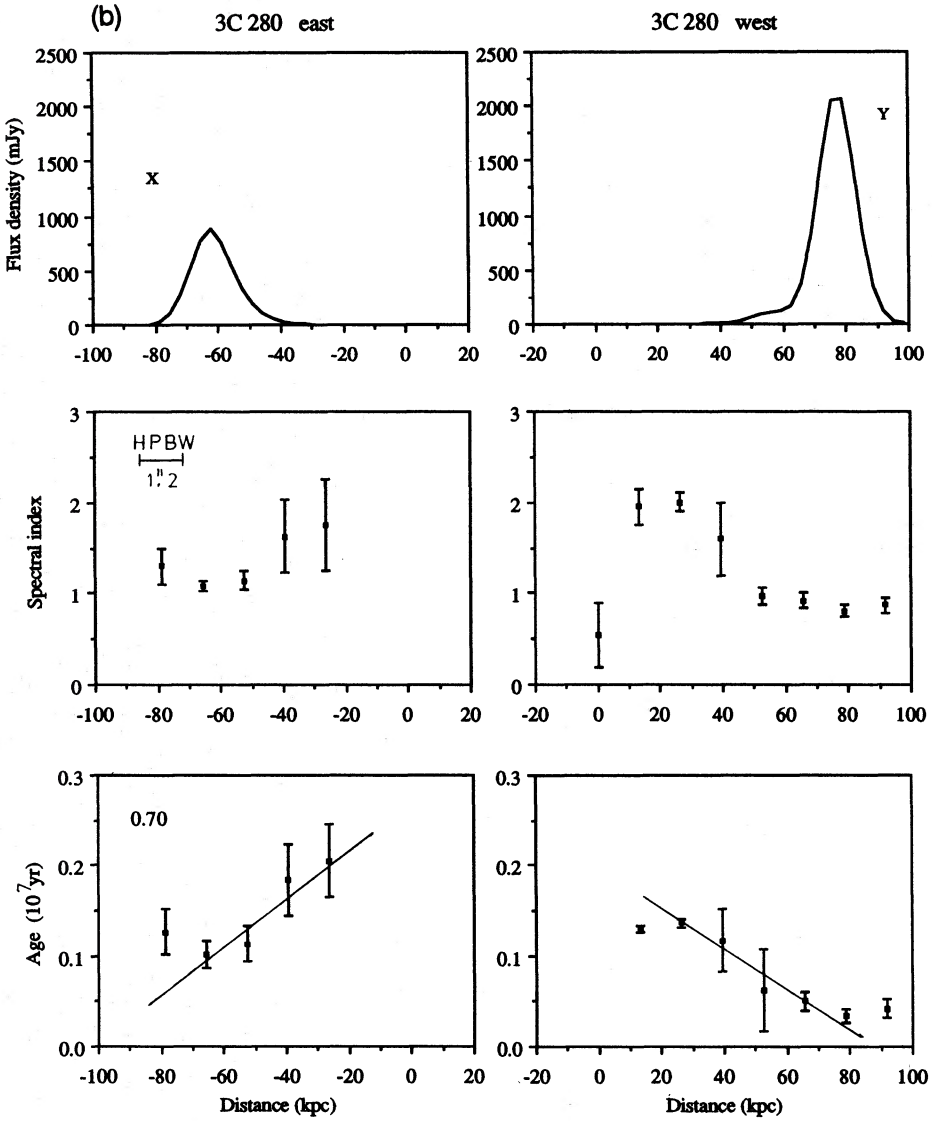

Figure 13 – *continued*

properties from the distorted lobes, nor do they have different separation speeds. This suggests that the outflow speeds must be comparable with or larger than the advance speed of the hotspot.

6.2 Correlations

The spectral ageing analysis of this high-luminosity sample has been carried out in a manner consistent with that of AL for lower power doubles, and the results of the two groups are therefore directly comparable. Fig. 18 is a plot of the separation speed of one lobe against that of the other lobe. Some sources have the parameters of only one lobe determined – they are therefore not plotted in this diagram. The sides called X correspond to those shown in Figs 4–17(a), and are chosen arbitrarily so that no physical selection bias is included. It is clear that the separation speeds of the two lobes of each source are strongly correlated.

Hereafter, when looking for correlations between the lobe separation speed and other properties of the source as a whole, we use the averaged lobe speed, $v=(v_x+v_y)/2$, for each source. AL correlated speed with power at 178 MHz for each lobe (P_L) and found that $v_{\rm lobe} \propto P_L^{0.33\pm0.13}$. Due to the facts that we have no direct measurement of the power of the individual lobes at 178 MHz, and that the two lobe speeds for each source are well correlated, we decided to use the averaged parameters for each source.

Fig. 19 plots v against P_{178}, the integrated radio power at 178 MHz. There are several features apparent in this plot.

(i) In the range 10^{27}–10^{28} W Hz^{-1} sr^{-1}, our results agree well with those of AL. The averaged lobe separation speed is significantly correlated with radio power, following a relation of the form $v \propto P_{178}^{0.4\pm0.1}$. For a flux-limited sample, redshift and luminosity are strongly correlated, so that the lobe speed is also correlated with redshift.

(ii) The apparent separation speeds now range up to $0.3c$. From our earlier discussion, we concluded that the speeds may be dominated by outflows from the hotspots rather than the advance speed of the hotspots, so the maximum figure of $0.3c$ is not directly comparable with those upper limits

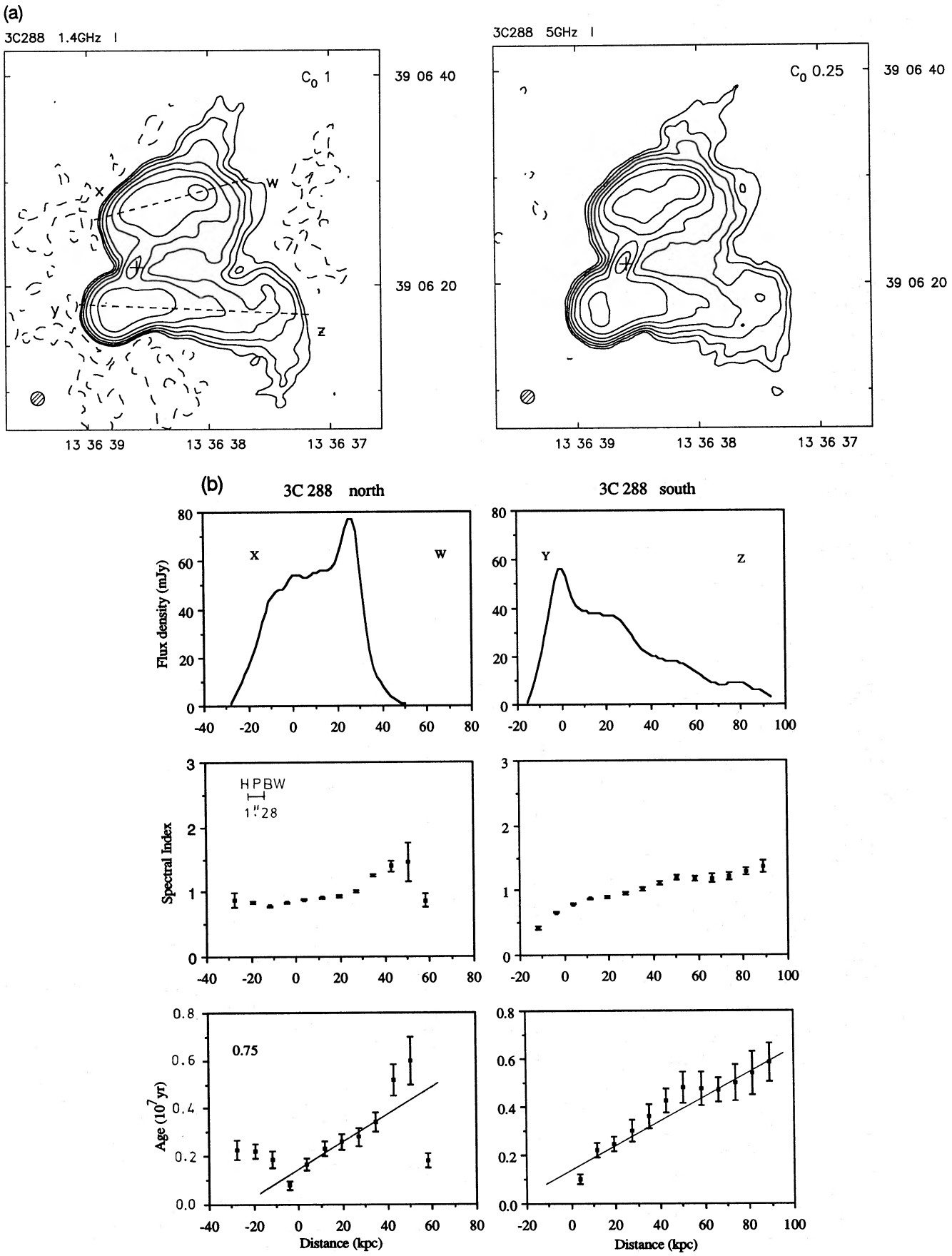

Figure 14. (a) Total intensity maps and (b) strip profiles of total intensity at 1.4 GHz, spectral index and age along the lobe axes indicated by the letters in (a), for 3C288. See the caption to Fig. 4 for further details.

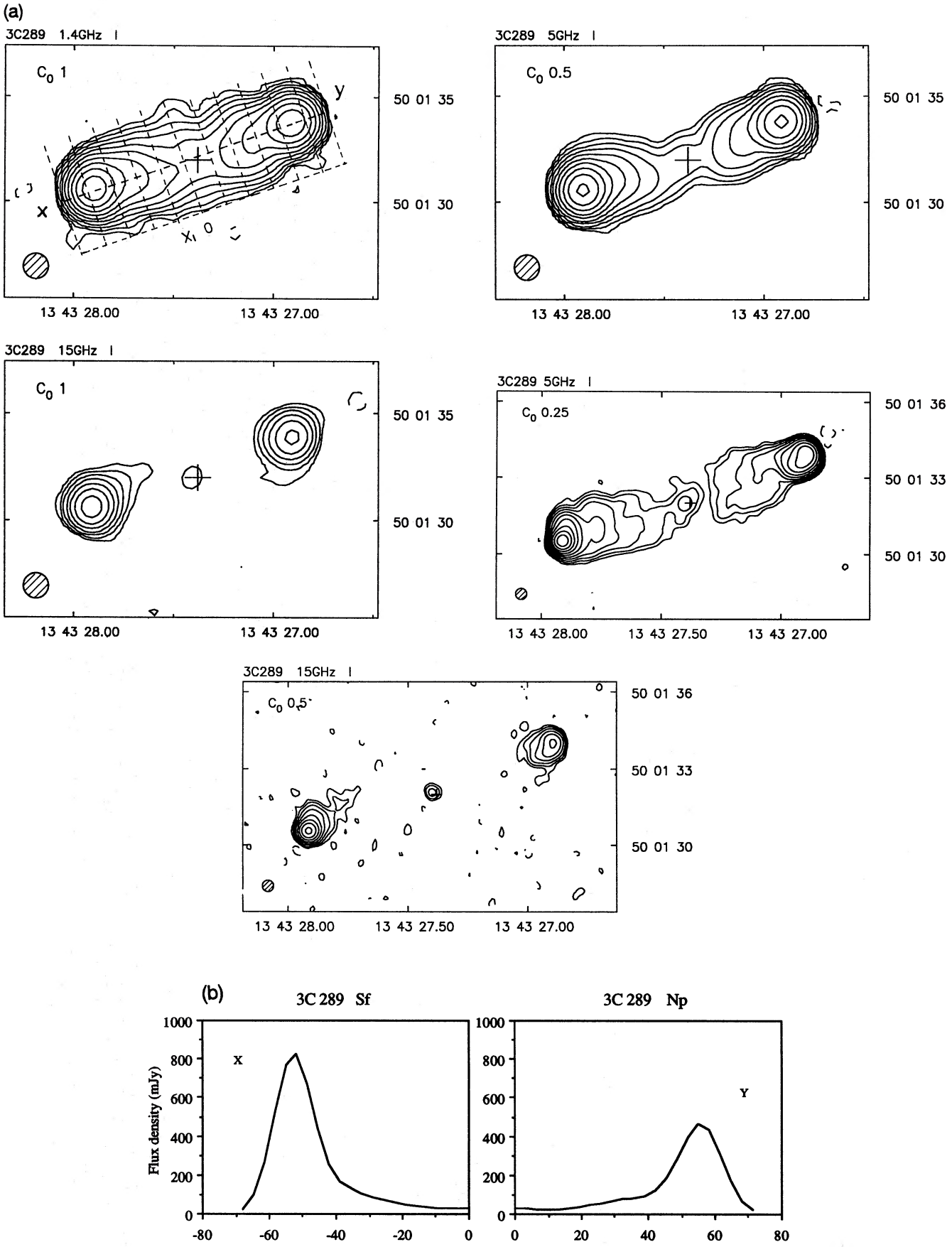

Figure 15. (a) Total intensity maps and (b) strip profiles of total intensity at 1.4 GHz, spectral index and age along the lobe axes indicated by the letters in (a), for 3C289. See the caption to Fig. 4 for further details.

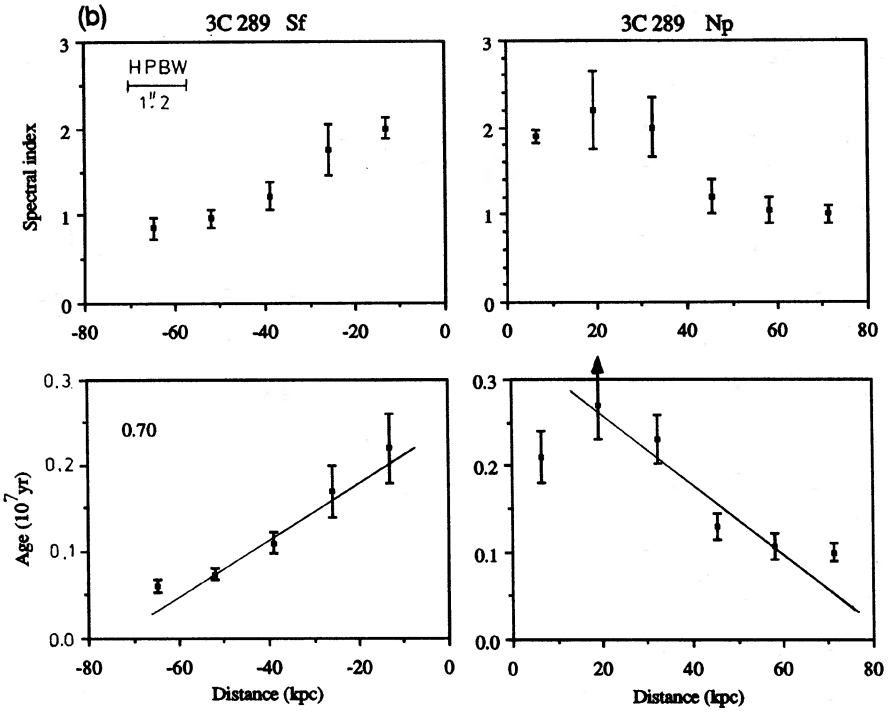

Figure 15 – *continued*

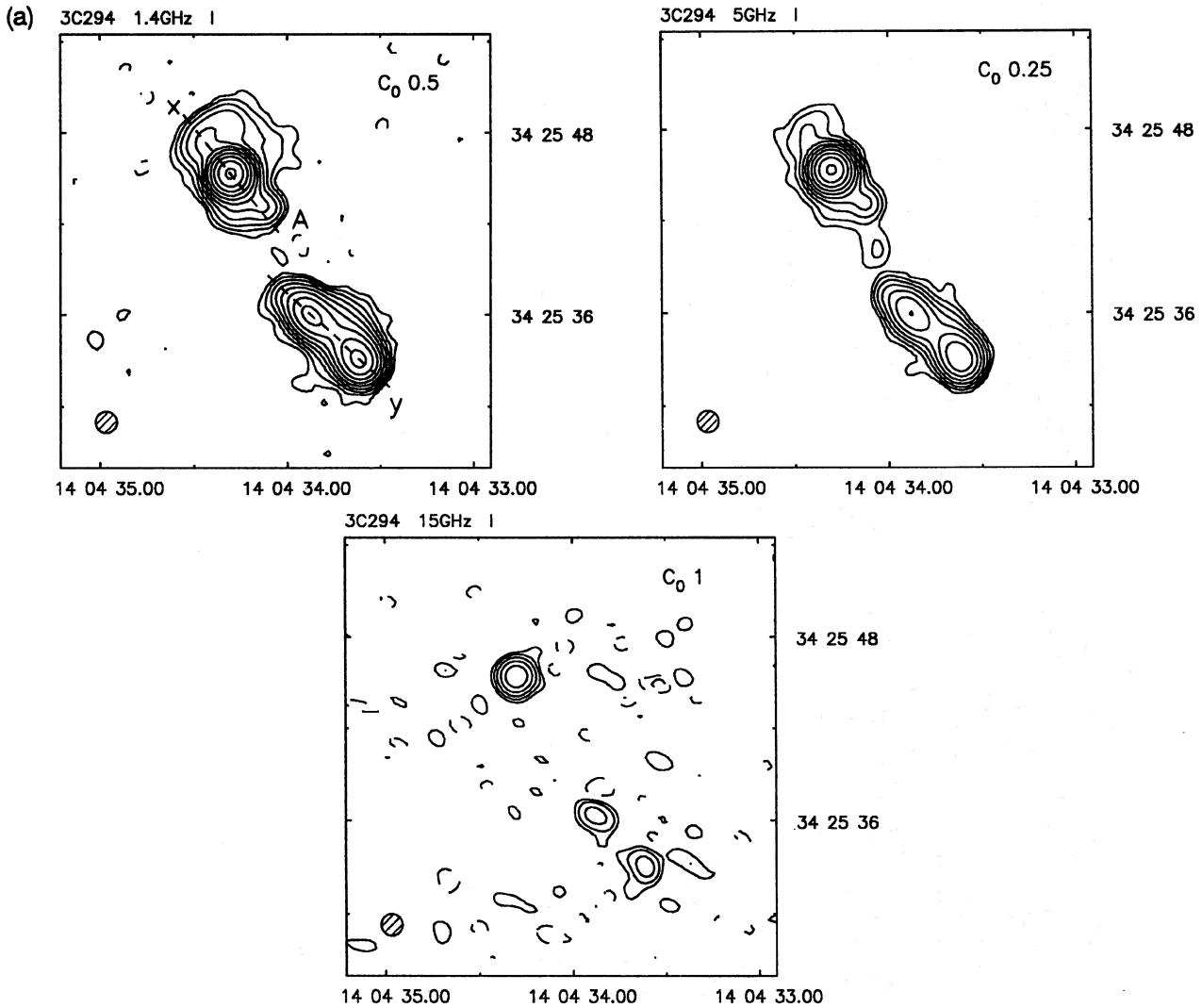

Figure 16. (a) Total intensity maps and (b) strip profiles of total intensity at 1.4 GHz, spectral index and age along the lobe axes indicated by the letters in (a), for 3C294. See the caption to Fig. 4 for further details.

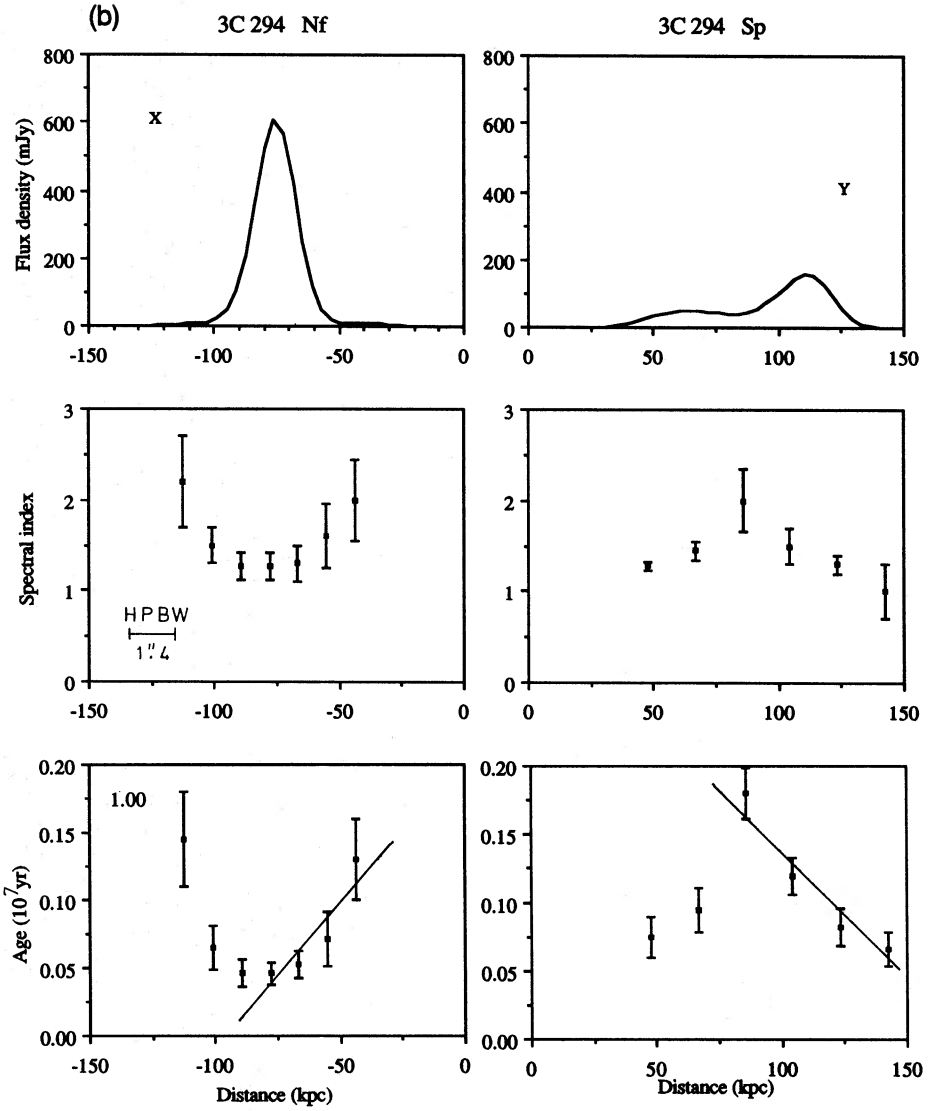

Figure 16 – *continued*

derived from brightness and angular-size ratios (Mackay 1973; Longair & Riley 1979; Swarup & Banhatti 1981).

(iii) To show how these results compare with those for FRI sources, we include in the plot speeds for three FRI sources (the filled squares) which have been analysed using the same method. They are 3C465 from Leahy (1984) and 0648+19B and 0648+19C from Liu *et al.* (1989). Their speeds are comparable with the lowest speeds for the double sources, at $\sim 0.01\ c$.

The minimum energy calculation gives $B_{\rm eq} \propto P^{1/2} D^{-1}$. Fig. 20 shows the dependence of the equipartition magnetic flux density of the source (averaged over the two lobes) upon radio luminosity. It shows a strong trend for $B_{\rm eq}$ to increase with luminosity. For a sample of sources with constant physical size and $B_{\rm eq} \gg B_{\rm MWB}$, this would lead to a strong v–P correlation of the type observed.

In order to illustrate this point we have used a magnetic flux density in the source equal to the equivalent $B_{\rm MWB}$. All but one of the sources now show $v_{\rm lobe} \leq 0.1c$, and the correlation with P_{178} is now weak (Fig. 21).

Naively one might expect that the larger sources would have the higher velocities. Fig. 22 plots the largest linear size, D, against v and shows that this is not the case. In fact, because of the strong $v-P$ correlation and the $P-D$ track, there should be a negative correlation between D and v; a lower bound is indeed seen on the $D-v$ diagram. Yet we also note from this diagram that the high apparent speeds are not confined to physically small sources.

6.3 Comments on the technique

The derived spectral age and thus the lobe separation speed are strongly dependent on the assumed magnetic flux density of the source, especially for the higher power sources where $B_{\rm eq}$ is on average 4–5 times higher than $B_{\rm MWB}$. We have used the equipartition arguments to derive the magnetic field in the source. The weakness of this approach includes the lack of evidence for equipartition and the uncertainties in the calculation, especially the source filling factor.

We have used a filling factor of unity so far. High-resolution observations of Cyg A with high dynamic range (Perley,

(a)

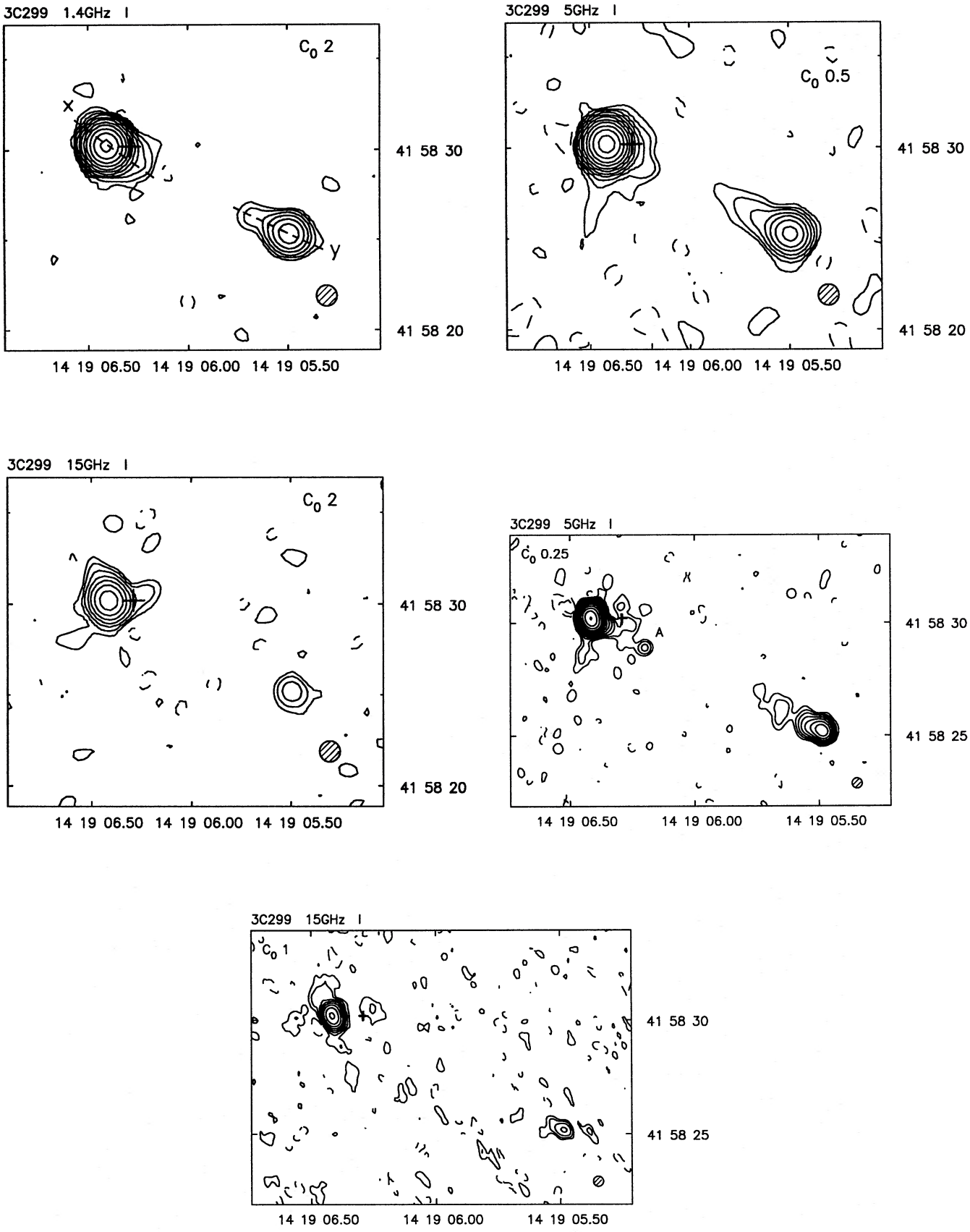

Figure 17. (a) Total intensity maps and (b) strip profiles of total intensity at 1.4 GHz, spectral index and age along the lobe axes indicated by the letters in (a), for 3C299. See the caption to Fig. 4 for further details.

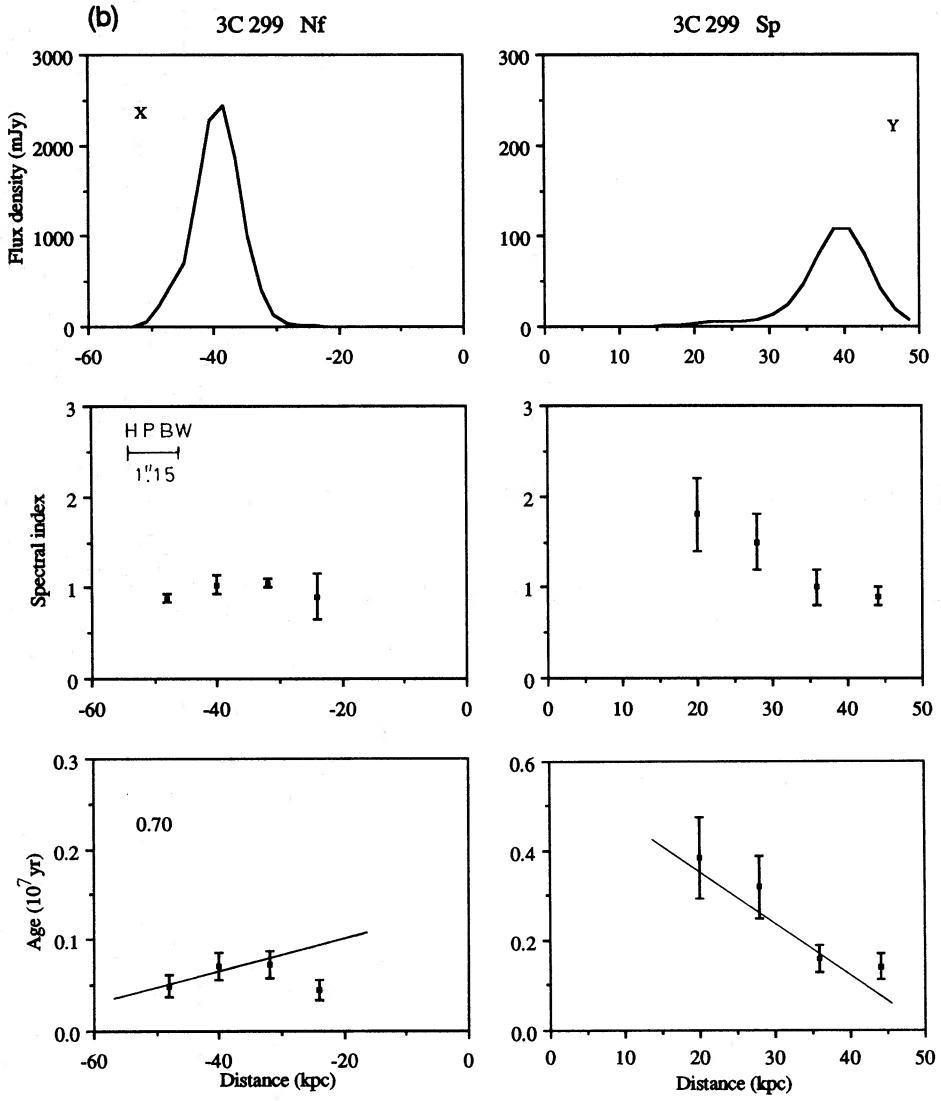

Figure 17 - *continued*

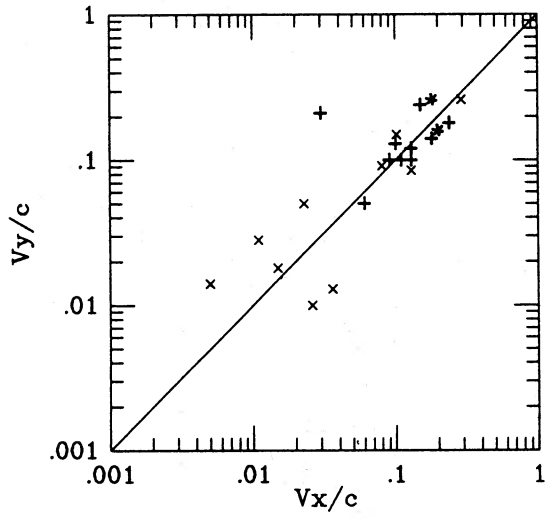

Figure 18. Logarithmic plot showing the correlation between the two lobe speeds for each source. The bold crosses and stars are the results for the current sample, where stars indicate the data from 5- and 15-GHz maps. Thin crosses are data from AL.

Dreher & Conway 1984) give a filling factor of 0.03–0.3. Low filling factors raise estimates of the equipartition magnetic fields, thus increasing the derived separation speed. If a filling factor of 0.1 is assumed, the magnetic field would be higher by a factor of 1.9. The separation speed, which scales with $[B_{\rm eq}^{1/2}/(B_{\rm eq}^2+B_{\rm MWB}^2)]^{-1}\sim B_{\rm eq}^{3/2}$ for the current higher luminosity objects [whose $B_{\rm eq}\sim(4\text{–}5)B_{\rm MWB}$], would thus be raised by a factor of 2.5. The upper limit on the lobe speed we derived here will become $0.75c$.

Another obvious factor which affects the apparent speed is the cosmological distance scale adopted. We use a Friedmann cosmology with $H_0=50$ km s^{-1} Mpc^{-1} and $q_0=0$. The dependence on H_0 of the derived parameters can be represented by a scaling factor $h_{50}=H_0/(50$ km s^{-1} Mpc$^{-1})$. The distance scales with h_{50}^{-1} and $B_{\rm eq}$ as $h_{50}^{2/7}$. These lead to the dependence of the derived velocity upon H_0 as $h_{50}^{-4/7}$. For instance, a value of H_0 of 100 km s^{-1} Mpc^{-1} will reduce the speed by a factor of 0.7.

7 CONCLUSIONS

From analysis of the variations of spectral index and age

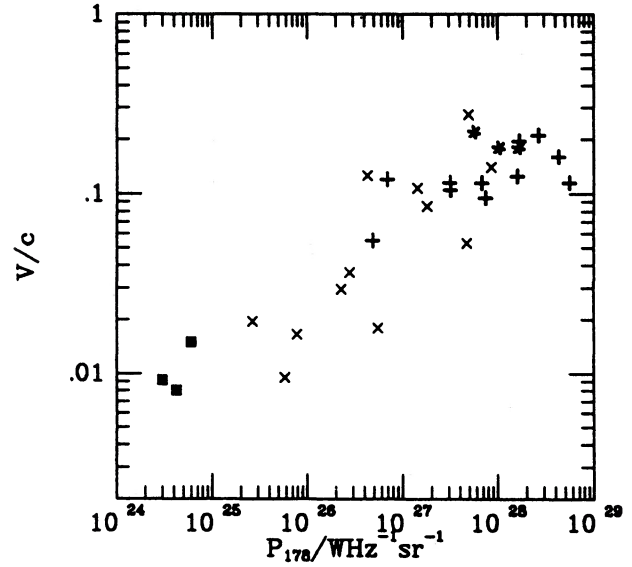

Figure 19. Logarithmic plots of the averaged lobe speed against luminosity. Filled squares are the spectral ageing results for three tailed sources (3C465, 0648 + 19 B and C). Other symbols as in Fig. 18.

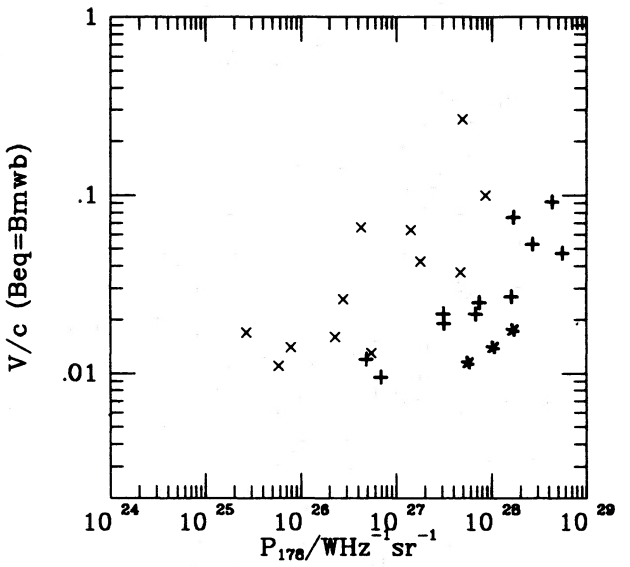

Figure 21. Logarithmic plot of the averaged lobe speeds, using the equivalent B_{MWB} as the magnetic flux density of the source, against luminosity. It shows a weaker $v-P$ correlation than that in Fig. 19. Symbols as in Fig. 19.

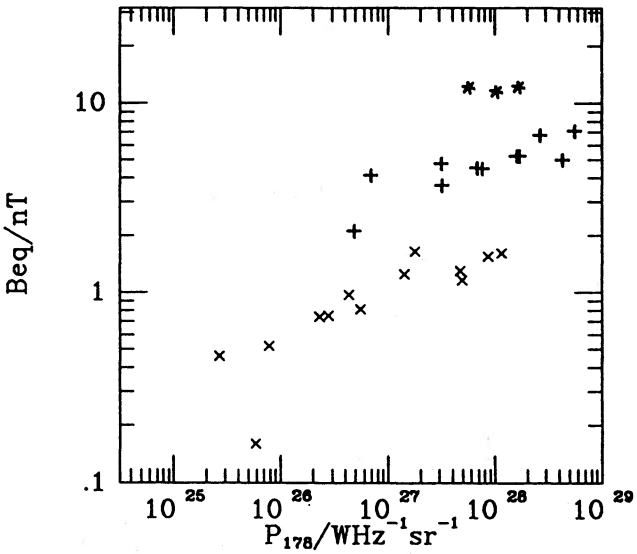

Figure 20. Logarithmic plot of the equipartition magnetic field against luminosity. Symbols as in Fig. 18.

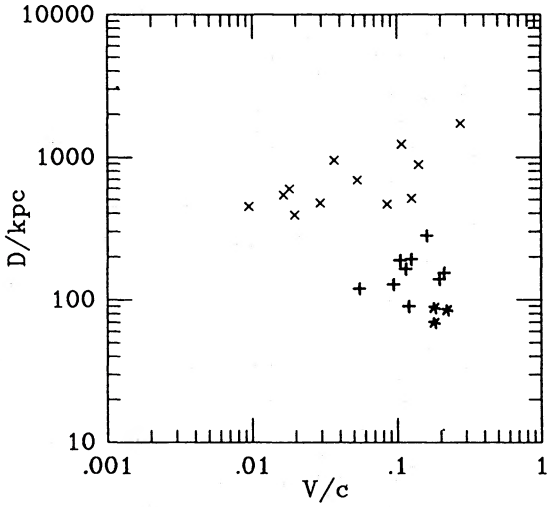

Figure 22. Logarithmic plot of the averaged lobe speed against largest linear size for the samples. Symbols as in Fig. 18.

across the lobes of an unbiased sample of classical double radio sources, the properties of the radio spectra have been derived. The main results are as follows.

(i) The high-luminosity sources exhibit a wide range of structures. Most of them do not conform to the classic backflow structures of FRII sources. The low-brightness extensions point towards and away from the nucleus, or transverse to the source axis.

(ii) The structural variations are connected with those of spectra. First, the spectra are indeed always flatter in the hotspots, and steepen into the diffuse lobe emission. Secondly, and more interestingly, this steepening is independent of the direction in which the lobe emission extends.

(iii) The steepening in the high-frequency radio spectra across the lobes is well interpreted in terms of synchrotron ageing, from which we derive a speed which separates the hotspot and a parcel of lobe material. The separation speed increases with radio power, and reaches as high as $0.3c$.

(iv) The lobe–hotspot separation speed is, in the classical doubles, a combination of the hotspot advance speed and the backflow velocity; in the distorted lobes it is the speed of outflow of the material from the hotspot. We find no significant difference in the separation speeds between the classic and the distorted lobes and hence conclude that the outflow

speeds from the hotspots frequently equal or exceed the hotspot advance speeds.

ACKNOWLEDGMENTS

We thank the Director and staff of the National Radio Astronomy Observatory for the observing time and their assistance; the NRAO is operated by Associated Universities, Inc., under contract with the National Science Foundation.

REFERENCES

Alexander, P., 1987. *Mon. Not. R. astr. Soc.,* **225,** 27.
Alexander, P. & Leahy, J. P., 1987. *Mon. Not. R. astr. Soc.,* **225,** 1 (AL).
Alexander, P., Brown, M. T. & Scott, P. F., 1984. *Mon. Not. R. astr. Soc.,* **209,** 851.
Baars, J. W. M., Genzel, R., Pauliny-Toth, I. I. K. & Witzel, A., 1977. *Astr. Astrophys.,* **61,** 99.
Barthel, P. D. & Miley, G. K., 1988. *Nature,* **333,** 319.
Blandford, R. D. & Rees, M. J., 1974. *Mon. Not. R. astr. Soc.,* **169,** 395.
Bridle, A. H., Fomalont, E. B., Byrd, G. G. & Valtonen, M. J., 1989. *Astr. J.,* **97,** 674.
Burch, S. F., 1977. *Mon. Not. R. astr. Soc.,* **180,** 623.
Burch, S. F., 1979. *Mon. Not. R. astr. Soc.,* **186,** 519.
Davis, R. J., Stannard, D. & Conway, R. G., 1983. *Mon. Not. R. astr. Soc.,* **205,** 1267.
Fanaroff, B. L. & Riley, J. M., 1974. *Mon. Not. R. astr. Soc.,* **167,** 31P.
Foley, A. R. & Barthel, P. D., 1990. *Astr. Astrophys.,* **228,** 17.
Fomalont, E. B. & Bridle, A. H., 1983. *The AIPS Cookbook,* NRAO, Charlottesville.
Harris, D. E., 1974. *Astr. J.,* **79,** 1211.
Hintzen, P., 1984. *Astrophys. J. Suppl.,* **55,** 553.
Hough, D. H. & Readhead, A. C. F., 1989. *Astr. J.,* **98,** 1208.
Jaffé, W. J. & Perola, G. C., 1973. *Astr. Astrophys.,* **26,** 423.
Laing, R. A., 1988. In: *Hotspots in Extragalactic Radio Sources,* p. 27, eds Meisenheimer, K. & Röser, H.-J., Springer-Verlag, Berlin.
Laing, R. A. & Peacock, J. A., 1980. *Mon. Not. R. astr. Soc.,* **190,** 903 (LP).
Laing, R. A., Riley, J. M. & Longair, M. S., 1983. *Mon. Not. R. astr. Soc.,* **204,** 151.
Leahy, J. P., 1984. *Mon. Not. R. astr. Soc.,* **208,** 323.
Leahy, J. P., Muxlow, T. W. & Stephens, P. W., 1989. *Mon. Not. R. astr. Soc.,* **239,** 401.
Liu, R. & Pooley, G. G., 1990. *Mon. Not. R. astr. Soc.,* **245,** 17P.
Liu, R. & Pooley, G. G., 1991a. *Mon. Not. R. astr. Soc.,* **249,** 343.
Liu, R. & Pooley, G. G., 1991b. *Mon. Not. R. astr. Soc.,* **253,** 669.
Liu, R., Riley, J. M., Warner, P. J., Pooley, G. G. & Alexander, P., 1989. *Mon. Not. R. astr. Soc.,* **240,** 501.
Longair, M. S. & Riley, J. M., 1979. *Mon. Not. R. astr. Soc.,* **188,** 625.
Mackay, C. D., 1973. *Mon. Not. R. astr. Soc.,* **162,** 1.
Mayer, C. J., 1979. *Mon. Not. R. astr. Soc.,* **186,** 199.
McCarthy, P. J., van Breugel, W., Spinrad, H. & Djorgovski, S., 1987. *Astrophys. J. Lett.,* **321,** L29.
McCarthy, P. J., Spinrad, H., van Breugel, W., Liebert, J., Dickinson, M., Djorgovski, S. & Eisenhardt, P., 1990. *Astrophys. J.,* **365,** 487.
Miley, G. K., 1980. *Ann. Rev. Astr. Astrophys.,* **18,** 165.
Myers, S. T. & Spangler, S. R., 1985. *Astrophys. J.,* **291,** 52.
Owen, F. N. & Puschell, J. J., 1984. *Astr. J.,* **89,** 932.
Pacholczyk, A. G., 1970. *Radio Astrophysics,* Freeman, San Francisco.
Perley, R. A., Dreher, J. W. & Conway, J. J., 1984. *Astrophys. J. Lett.,* **285,** L35.
Riley, J. M. & Pooley, G. G., 1975. *Mem. R. astr. Soc.,* **80,** 105.
Stocke, J. T., Burns, J. O. & Christiansen, W. A., 1985. *Astrophys. J.,* **299,** 799 (SBC).
Swarup, G. & Banhatti, D. G., 1981. *Mon. Not. R. astr. Soc.,* **194,** 1025.
Winter, A. J. B., Wilson, D. M. A., Warner, P. J., Waldram, E. M., Routledge, D., Nicol, A. T., Boysen, R. C., Bly, D. W. J. & Baldwin, J. E., 1980. *Mon. Not. R. astr. Soc.,* **192,** 931.
Wyndham, J. D., 1966. *Mon. Not. R. astr. Soc.,* **144,** 459.